Supporting Information for Publication

Specific features of supramolecular organisation and hydrogen bonding in proline cocrystals: a case study of fenamates and diclofenac

Artem O. Surov[1,*], Alexander P. Voronin[1], Mikhail V. Vener[2], Andrei V. Churakov[3], German L. Perlovich[1].

[1]G.A. Krestov Institute of Solution Chemistry of the Russian Academy of Sciences, 1, Akademicheskaya St., 153045 Ivanovo;

[2]Mendeleev University of Chemical Technology, 9, Miusskaya Square, 125047 Moscow, Russia;

[3]N.S. Kurnakov Institute of General and Inorganic Chemistry of the Russian Academy of Sciences, Leninsky pr., 31, 119991, Moscow, Russia.

Table of contents

S1. Materials and Methods

S1.1. Compounds and solvents

All the fenamates, diclofenac sodium and L-proline (>99% purity) were available commercially and were used without further purification. Diclofenac sodium was neutralised with HCl to obtain free diclofenac acid. Before co-crystallisation experiments, all the substances were characterised by X-ray powder diffraction (XRPD) and compared with the XRPD patterns calculated based on their single crystal structure data. Mefenamic, tolfenamic acids and clonixin were identified as form I (ref. codes XYANAC and KAXXAI01, BIXGIY). The experimental XRPD pattern of diclofenac acid was found to be in good agreement with form II (SIKLIH07) The solvents were obtained from various suppliers and used as received without further purification.

S1.2 Screening procedures

S1.2.1 Screening by Differential Scanning Calorimetry (DSC)

In the typical DSC screening experiment, a physical mixture of fenamate and L-proline were placed in a 2 mL test tube in 1:1 molar ratio and mixed with a vortex mixer for 1 min. The final mixture was immediately loaded to the aluminum pans and subjected to DSC analysis.

S1.2.2 Grinding experiments

The grinding experiments were performed using a Fritsch planetary micro mill, model Pulverisette 7, in 12 ml agate grinding jars with ten 5 mm agate balls at a rate of 500 rpm for 40 min. In a typical experiment, 80 mg of fenamate and L-proline in a 1:1 molar ratio were placed in a grinding jar, and 60 μl of solvent was added with a micropipette.

S1.3 Slurry and solution crystallization

The bulk samples of the cocrystals was obtained by stirring a slurry of components (200 mg) in a 1:1 molar ratio in ethanol for 24 hours at room temperature. The resulting material was air-dried and subjected to DSC and XRPD analyses.

In the solution crystallisation experiments, fenamate (80 mg) was dissolved with L-proline in 1:1, 1:2 and 2:1 molar ratios in ethanol, methanol or acetone and stirred at room temperature until a clear solution was obtained. The resulting solutions were filtered into a 10 ml vial, covered by a parafilm perforated with a few small holes, and allowed to evaporate slowly until a crystalline material was formed. Good quality single crystals of the fenamate + L-proline cocrystals were obtained from the ethanol.

S1.4 X-ray diffraction experiments

Single-crystal X-ray diffraction data were collected on a Bruker SMART APEX II diffractometer using graphite-monochromated MoKα radiation (λ = 0.71073 Å).[1] Absorption corrections based on measurements of equivalent reflections were applied. The structures were solved by direct methods and refined by full matrix least-squares on F^2 with anisotropic thermal parameters for all the non-hydrogen atoms.[2] All the hydrogen atoms were found from a difference Fourier map and refined isotropically. The crystallographic data for the [**CLX+Pro**] (1:1), [**Dic+Pro**] (1:1) and [**NFA+Pro**] (1:1) cocrystal have been deposited with the Cambridge Crystallographic Data Centre as supplementary publications under CCDC numbers 1863144-1863146. This information may be obtained free of charge from the Cambridge Crystallographic Data Centre via www.ccdc.cam.ac.uk/data_request/cif.

The X-ray powder diffraction (XRPD) data of bulk materials were recorded under ambient conditions in Bragg-Brentano geometry with a Bruker D8 Advance diffractometer with $CuK\alpha_1$ radiation (λ = 1.5406 Å).

S1.5 Thermal analysis

Thermal analysis was carried out using a *Perkin Elmer* DSC 4000 differential scanning calorimeter with a refrigerated cooling system (USA). The sample was heated in sealed aluminum pans at the rate of 10 $K \cdot min^{-1}$ in a nitrogen atmosphere. The unit was calibrated with indium and zinc standards. The accuracy of the weighing procedure was ±0.01 mg.

S1.6 Infrared Spectroscopy (IR)

Fourier-transform infrared spectra of the cocrystals and pure compounds were recorded on a FTIR spectrometer Bruker Vertex V80. All the samples were pressed into KBr pellets and recorded at frequencies from 4000 to 350 cm^{-1}.

S1.7 Solubility experiments

S1.7.1 Solubility of pure compounds

The solubility of fenamate drugs was measured by the shake-flask method in phosphate buffer at pH6.8 at 25.0± 0.1°C. The excess amount of each compound was suspended in 2 ml of the solvent and allowed to equilibrate under shaking for 48 hours. An aliquot of the suspension was filtered using a 0.2 μm filter (Rotilabo® syringe filter, PTFE), and the concentration of fenamate was determined with a suitable dilution by a Cary 50 UV-vis spectrophotometer (Varian, Australia) at

the reference wavelength. The results are stated as the average of at least three replicated experiments.

S1.7.2 Measurement of cocrystal solubility

The equilibrium solubility of the cocrystals was estimated at the eutectic point, where the drug and cocrystal solid phases are in equilibrium with the solution.[3] In order to assess the eutectic point between the drug and the cocrystal, a series of L-proline solutions (pH 6.8) were prepared. Excess amount of fenamate was added into a vial with 1ml of each of the prepared L-proline solutions and allowed to equilibrate under shaking for 5 days at 25.0±0.1°C. After the equilibration, the composition of solid residues recovered after the experiment was analysed by DSC and PXRD. The eutectic point of a cocrystal were determined in the solution with the lowest L-proline concentration, which were confirmed to have a mixture of two solid phases (drug and cocrystal), coexisting in equilibrium with solution. The concentration of fenamate in the eutectic point was analysed by a Cary 50 UV-vis spectrophotometer (Varian, Australia) at the reference wavelength. Since L-proline cannot be detected by UV-vis spectroscopy, its concentration at the eutectic point was assume to be equal to the initial concentration of the prepared L-proline solutions.

S2 Computational details

S2.1 Solid-state DFT calculations

The DFT calculations of the cocrystals were performed with the CRYSTAL14 software[4] using B3LYP functional with the Grimme D2 dispersion correction[5] and 6-31G(d,p) basis set. Before the optimisation of atom positions, the X-H distances were normalised to their standard neutron diffraction values. The space group and unit cell parameters were taken from experiment and kept fixed during energy minimisation. The influence of the dispersion correction type on the structures and IR spectra of cocrystals was studied by us on the example of [CLX+Pro], for which the DFT calculations were also performed using the Grimme D3(BJ) correction[6, 7] in the CRYSTAL17 program.[8] According to the packing similarity analysis performed in Mercury,[9] the relaxed geometries calculated with the D2 and D3 correction are highly close to each other (rmsd(15)=0.023).

The Bader analysis of periodic electron density[10] was performed using TOPOND14 [m7], and the search for (3;-1) critical points was conducted between the pairs of atoms within the 5Å radius. The following electron-density features at the bond critical point were computed for every non-covalent interaction: (i) the values of the electron density, ρ_b, (ii) the Laplacian of the electron density, $\nabla^2\rho_b$, and (iii) the positively defined local electronic kinetic energy density, G_b. The lower threshold on ρ_b for (3;-1) points taken for consideration was 0.003 a.u.[11]

S2.2 Evaluation of the intermolecular interaction energies and cohesive energies

A common approach to cohesive energy estimation (E_{coh}) for the cocrystals is based on the total electronic energies of cocrystal and isolated molecules of its components obtained from DFT calculations:[12-14]

$$\mathrm{E}_{\mathrm{coh}} = \frac{E_{bulk} - \sum a_i E_i}{Z}, \quad \text{(s1)}$$

where $\mathrm{E}_{\mathrm{bulk}}$ is the total energy of a system, Z is number of molecules in the unit cell, a_i is number of symmetrically equivalent molecules of each type in the unit cell, E_{i} is the energy of an isolated molecule extracted from the bulk after optimisation. The E_{i} value includes SCF energy of isolated molecule with respect to dispersion and ZPVE correction, as well as counterpoise correction[15, 16] performed using the standard MOLEBSSE routine implemented in the CRYSTAL package.[4] In case of flexible molecules, an additional term E_{conf} is added which reflects the difference in stable conformations in bulk and in gas phase. With regard to this, equation (2) can be written as:

$$\mathrm{E}_{\mathrm{coh}} = \frac{E_{bulk} - \sum_i a_i (E_i + BSSE_i - E_{conf,i})}{Z}, \quad \text{(s2)}$$

For the presented scheme to be true, the value of BSSE correction is considered additive:

$$BSSE = \sum_i BSSE_i \quad \text{(s3)}$$

and virtually constant during optimisation of isolated molecules. Since the molecules of all APIs studied in present work are conformationally flexible, and L-Proline undergoes intramolecular proton transfer upon transition from crystal to gas phase, the applicability of Eq. (s3) to the considered crystals is unclear. Therefore, we considered additive schemes to $\mathrm{E}_{\mathrm{coh}}$ evaluation as a promising alternative to equation (s3).

In the approach used in the present article, the energy of the particular noncovalent interaction, $\mathrm{E}_{\mathrm{int}}$, is evaluated from the Bader analysis of periodic electron density according to following equation:[17]

$$E_{\mathrm{int}}\ (\mathrm{kJ \cdot mol^{-1}}) = 1147 \cdot G_{\mathrm{b}}\ (\mathrm{a.u.}) \quad \text{(s4)}$$

It yields reasonable E_{int} values for molecular crystals with different types of intermolecular interactions: H-bonds, C–H···O, Cl···Cl contacts, etc. [11, 18, 19]

An alternative way to estimate the strength of the H-bond is the relationship between the H-bond enthaply and the O···H distance known as Rozenberg equation[20]:

$$\Delta H_{H-bond} = 0.134 \cdot D(H \cdots O)^{-3.05} \quad \text{(s5)}$$

The cohesive energy is then estimated as sum of the unique non-covalent interaction energies in the pairs of atoms in the asymmetric unit:

$$E_{coh} = \sum_i \sum_{j<i} E_{\mathrm{int},j,i} \quad \text{(s6)}$$

where $E_{\mathrm{int},j,i}$ is the energy of a particular contact between the i-th atom and the j-th atom that belong

to different molecules.

The additive scheme based on equations (s4) and (s6) provides reasonable lattice energies for two-component molecular crystals, as shown in Refs.[21, 22]

S2.3 XPac analysis

The quantitative analysis of packing similarity was performed using XPac v. 2.0.2.[23] This method allows finding the isostructural supramolecular constructs within the pairs of crystals by comparing the relative position and orientation of identical molecular graphs named 'common sets of points' in clusters which imitate the crystal environment of a molecule. The measure of packing similarity is the dissimilarity index X, which shows the difference in angles δ_a and interplanar angles δ_p, and stretch parameter D, which indicates the difference in distances between the nearest identical fragments. Lattice parameters and positions of all heavy atoms used in the calculation were taken from the X-Ray experiment. A cluster of 15 molecules with intermolecular atom-atom distance shorter than sum of van-der-Waals radii of contact atoms + 1.5 Å was considered for each crystal. Medium-level threshold values for parameters δ_a and δ_p were used, which equals 10° and 14°, respectively.

S2.4 1D periodic calculations

Geometry optimisation of isolated ribbons and estimation of their cohesive energies was performed using 1D periodic DFT methods in CRYSTAL14 software suite by using the HELIX keyword at the same level of theory as for the corresponding crystals. In all cases, the structure of the ribbon was determined by the 2-fold screw axis ($P2_1$ symmetry). The O-H···O-bonded heterodimer extracted from the X-Ray determined crystal structure was used as a monomeric unit of the ribbon. The initial step of the ribbon was set equal to that in crystal. The cohesive energy E_{coh} of the ribbon was calculated by the QTAIMC approach, i.e. using eqs. (s4 and s5).

S3. Results

S3.1. Results of cocrystal screening

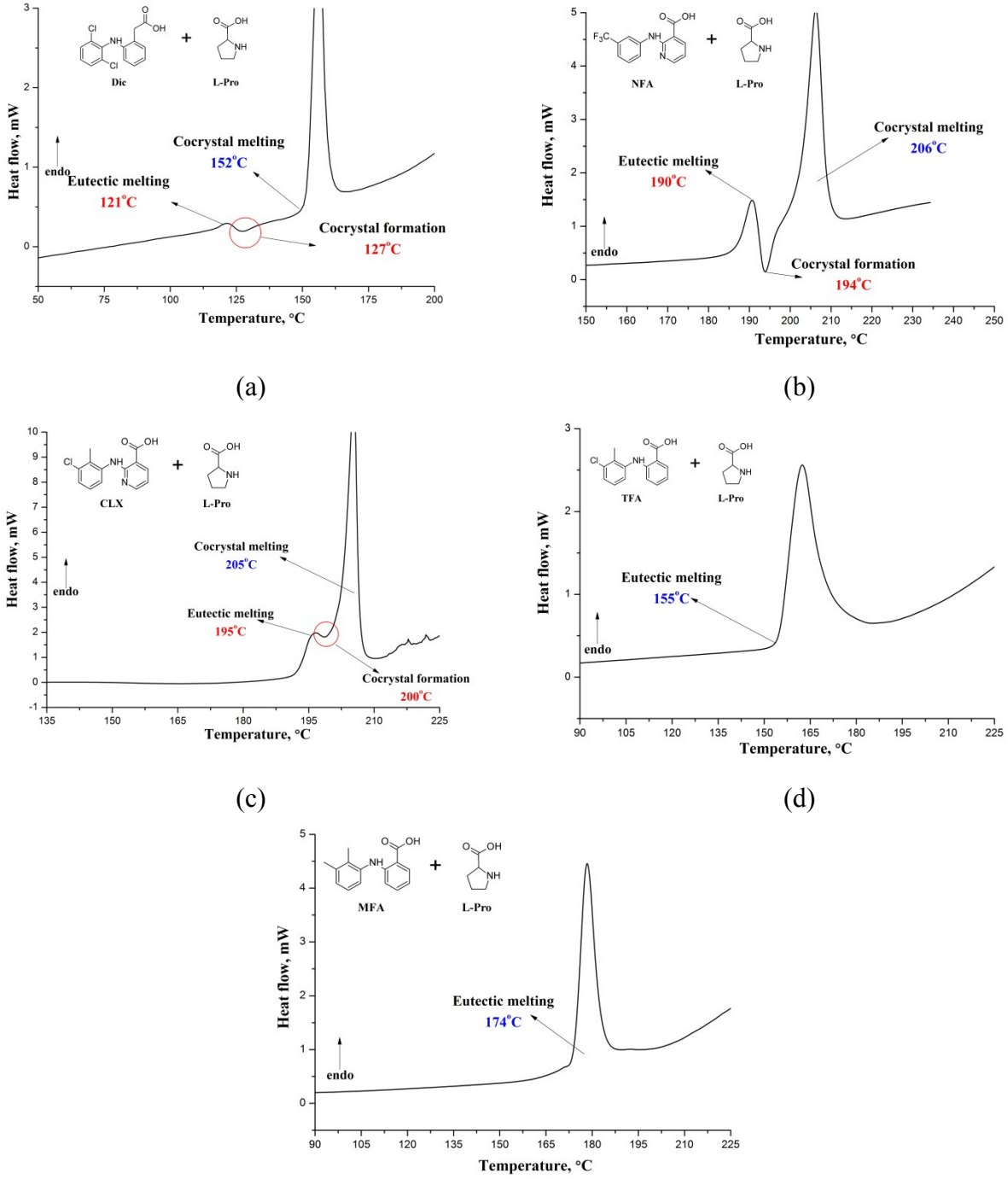

Fig. S1. DSC traces for fenamate + L-proline physical mixtures in 1:1 molar ratio recorded at at 10°C·min^{-1} heating rate: diclofenac + L-proline (a); niflumic acid + L-proline (b); clonixin + L-proline (c); tolfenamic acid + L-proline (d); mefenamic acid + L-proline (e).

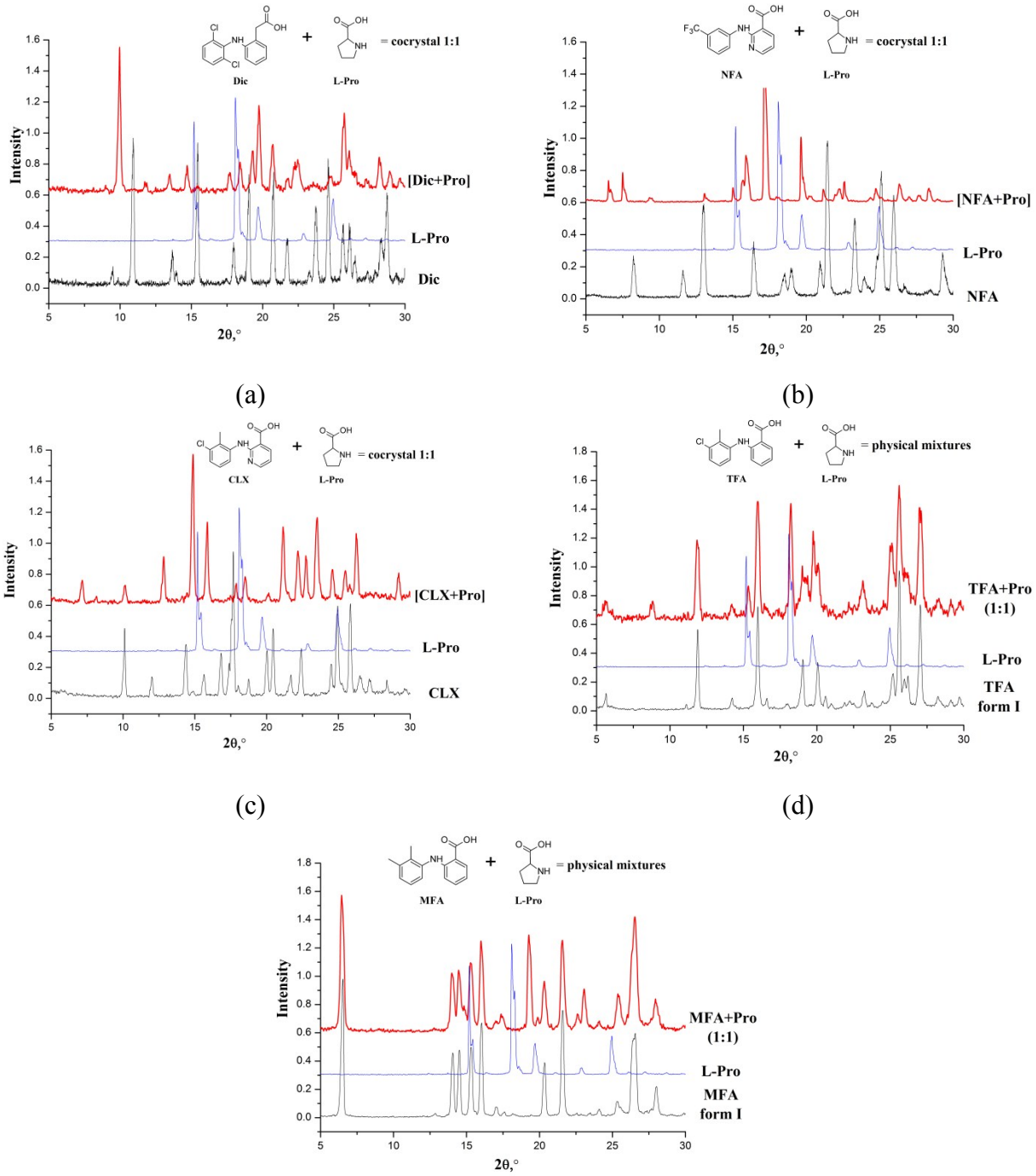

Fig. S2. Results of PXRD analysis of materials obtained by liquid-assisted grinding: diclofenac + L-proline (a); niflumic acid + L-proline (b); clonixin + L-proline (c); tolfenamic acid + L-proline (d); mefenamic acid + L-proline (e).

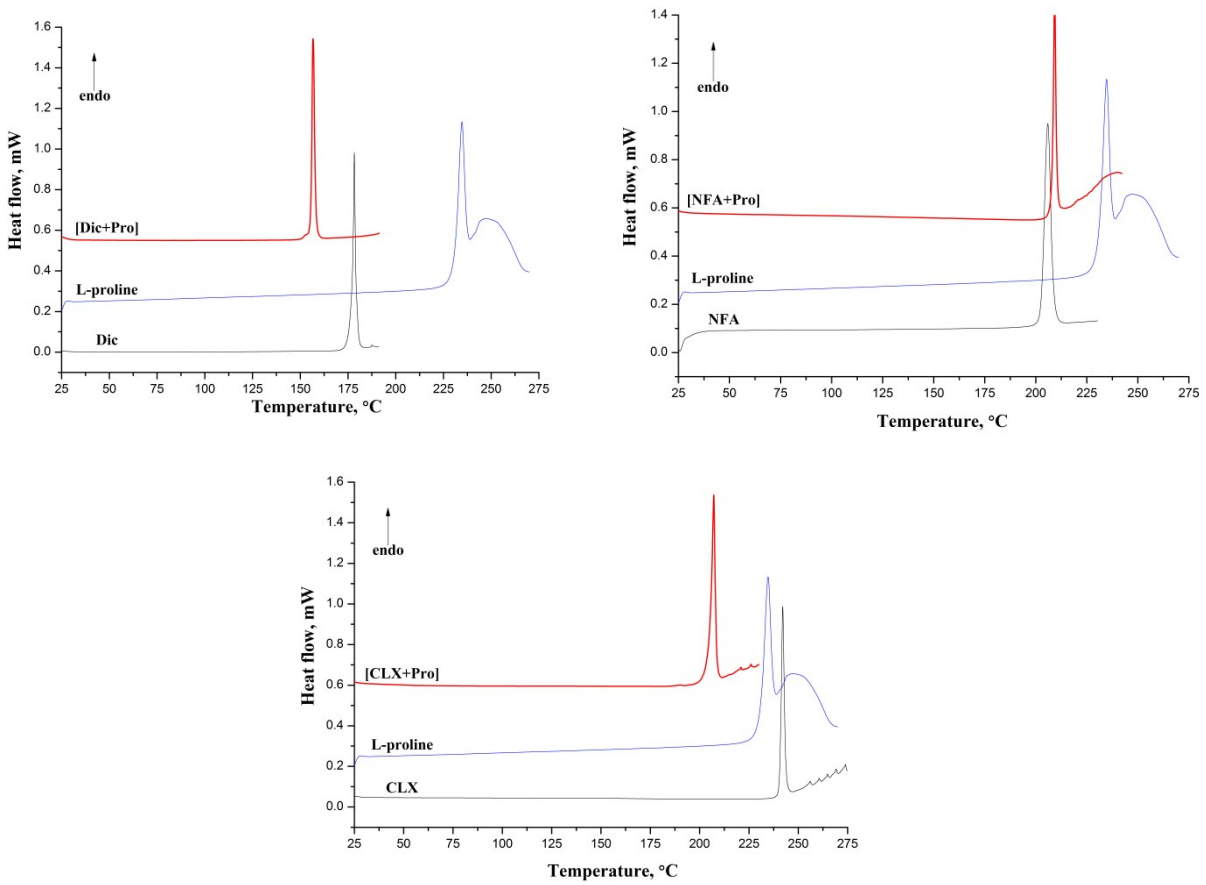

Fig. S3. DSC curves of **Dic**, **NFA**, **CLX**, L-proline and the corresponding cocrystals recorded at 10°C·min^{-1} heating rate.

S3.2 Crystal structure analysis and CSD survey

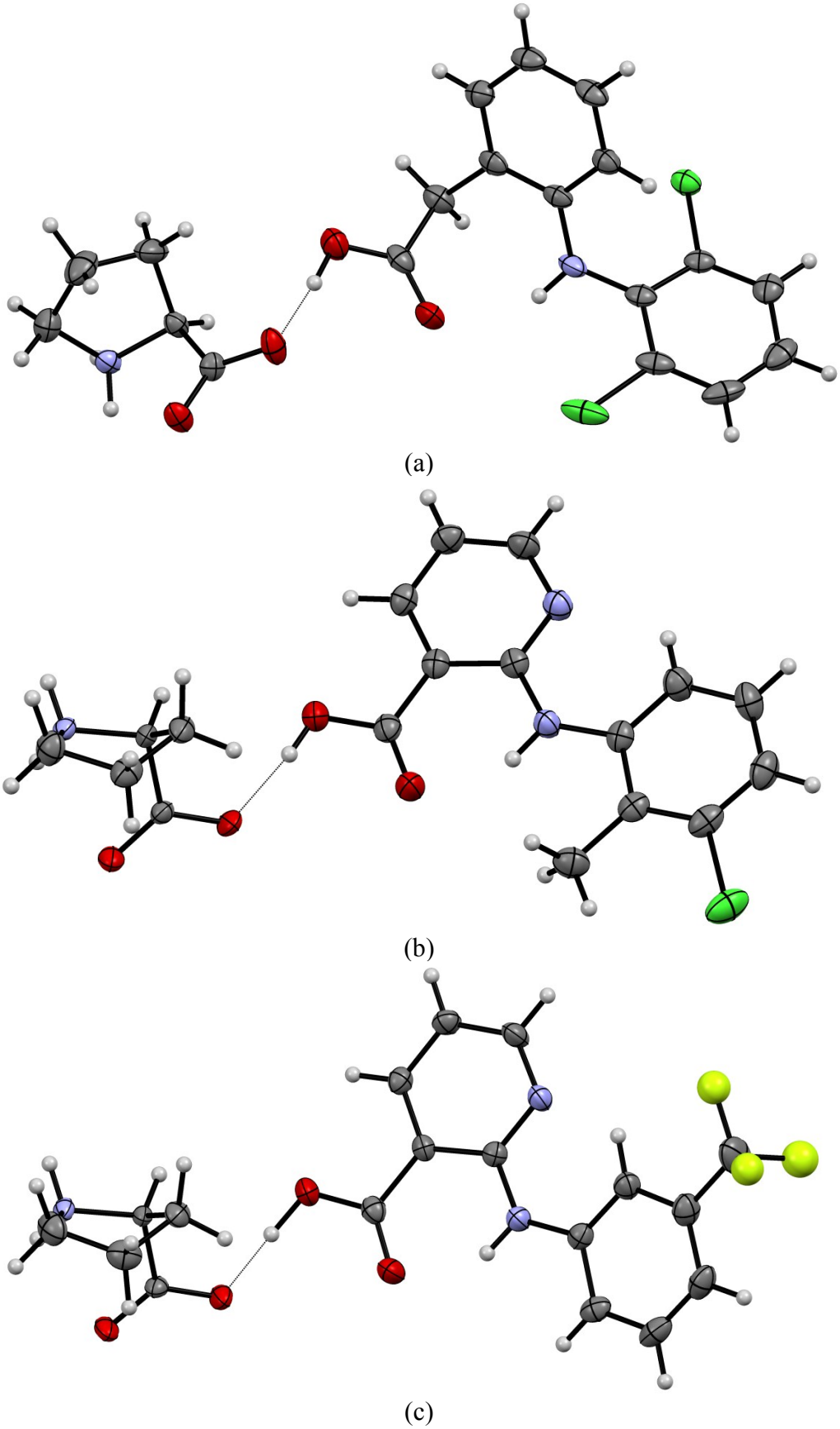

Fig. S4. ORTEP images of asymmetric units in the [**Dic+Pro**] (a), [**CLX+Pro**] (b) and [**NFA+Pro**] (c) cocrystals. The disordered fluorine atoms in the [**NFA+Pro**] crystal with low occupancy are removed for clarity.

Table S1. Some of the crystallographic data for the NSAID + L-proline cocrystals obtained in the present work

Cocrystal	[**Dic+Pro**] (1:1)	[**NFA+Pro**] (1:1)	[**CLX+Pro**] (1:1)
CCDC No.	1863145	1863146	1863144
Chemical formula	$C_{14}H_{11}Cl_2NO_2$•$C_5H_9NO_2$	$C_{13}H_9F_3N_2O_2$•$C_5H_9NO_2$	$C_{13}H_{11}ClN_2O_2$•$C_5H_9NO_2$
Crystal system	Monoclinic	Monoclinic	Orthorhombic
a (Å)	9.2716(9)	11.8073(17)	5.7721(7)
b (Å)	5.2277(5)	5.8122(8)	12.3373(15)
c (Å)	20.3473(19)	13.3488(19)	24.977(3)
α (°)	90.00	90.00	90.00
β (°)	102.235(1)	97.844(2)	90.00
γ (°)	90.00	90.00	90.00
Unit cell volume (Å^3)	963.82(16)	907.5(2)	1778.6(4)
T (K)	180(2)	180(2)	150(2)
Space group	$P2_1$	$P2_1$	$P2_12_12_1$
Z	2	2	4
Total number of relections	9301	10012	13863
Number of independent reflections	4183	2624	3213
R_{int}	0.0189	0.0229	0.0303
*R*1 [*I*>2 δ (*I*)]	0.0278	0.0514	0.0275
wR(F^2) (*I* > 2σ(*I*))	0.0650	0.1364	0.0626
Goodness-of-fit (on F^2)	1.045	1.062	1.045

General discussion on the XPac analysis

A row of 90 crystal structures containing the enantiopure proline (both L- and D-) in its zwitterionic form were extracted from the Cambridge Structural Database[24], including two polymorphic modifications (PROLIN03 and PROLIN04), a 1:1 hydrate (RUWGEV) and cocrystals with different compounds of various stoichiometry. When building the set of crystals for XPac analysis, we excluded from the consideration the structures containing racemic proline and inorganic ions. The final number of crystal structures chosen for the packing similarity analysis equals to 65 crystals from the CSD + 3 crystals from the present study, i.e 68 structures. Some structure information of crystals used in XPac analysis is presented in Table S2.

A proline zwitterion is relatively flexible due to the non-rigidness of the cyclic alkyl fragment. From the view of hydrogen bond topology, In the terms of hydrogen bond topology, the only important factor which determines the geometry of **Pro** is the mutual arrangement of the amino group and the carboxylate fragment. This value is determined by the rotation profile of the carboxyl group relative to the rest of the molecule and the interplanar angle describing the "slope" of the O-O-C-C plane with respect to the cyclic fragment. From the DFT calculations performed in Ref. [25], we can conclude that the rotation of the carboxylic group requires considerable energy costs. The differences in molecular structure associated with conformational mobility of cyclic fragment in Pro are less relevant to the packing in hydrogen-bonded crystals and need to be excluded from the consideration prior to XPac analysis. For this reason, we chose the fragment presented in Scheme S1 as a common set of points, which includes the atoms of the carboxylate group, the amino nitrogen, and the bridging carbon atom between these groups.

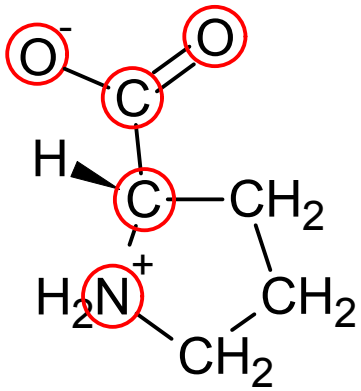

Scheme S1. Atoms in the **Pro** zwitterion chosen as common set of points for XPac analysis.

Table S2. Crystal structures used in the XPac analysis with features of supramolecular arrangement of Pro zwitterions.

Refcode/ID	D/L	Second component	Z'(API): Z'(Pro)[a]	Space group	Chain type[b]	Chain period	Double chain arrangement[c]	Interchain bond type[d]
[**CLX+Pro**][e]	L	Clonixin	1:1	$P\,2_1\,2_1\,2_1$	Z	5.7721	para	H-bonded
[**Dic+Pro**] [e]	L	Diclofenac acid	1:1	$P\,2_1$	C	5.2277	para	non-H-bonded
[**NFA+Pro**] [e]	L	Niflumic acid	1:1	$P\,2_1$	Z	5.8122	para	H-bonded
BEJNAI	L	Celecoxib	2:4	$P\,2_1\,2_1\,2_1$	other	5.016875	anti	H-bonded
BEXGUI	L	(R,S)-naproxen hydrate	2:2:2	$P\,2_1$	non-HB	-	-	-
CIDBOH	L	4-Aminobenzoic acid hydrate	1:2:1	$P\,2_1$	other	5.20835	anti	H-bonded-
CIPVUU	L	Dapagliflozin	4:8	P 1	Y/Z 3:1	5.667	anti	non-H-bonded
CIPZIM	L	Dapagliflozin	2:2	$P\,2_1\,2_1\,2_1$	Y/Z 1:1	5.7205	isolated	-
CIRFEQ	L	Dapagliflozin hydrate	4:4:2	P 1	Y	5.7695	isolated	-
DUKJUP	L	(S,R,R,R,S,S)-1-[3,5-bis(trifluoro-methyl)phenyl]-3-[(5-ethenyl-1-aza-bicyclo[2.2.2]octan-2-yl)-(6-methoxy-quinolin-4-yl)methyl]thiourea methanol solvate	1:1:1	$P\,2_1\,2_1\,2_1$	other	11.597	isolated	-
EJEPOA	L	Kaempferol	1:2	$P\,2_1$	Y	5.3597	anti	H-bonded
EJEPUG	L	Luteolin	1:1	$P\,2_1$	Z	5.7951	para	H-bonded
EJEQAN	L	Chrysin	1:1	$P\,2_1\,2_1\,2_1$	C	5.3011	para	non-H-bonded
EJEQER	L	Genistein	1:2	P 1	C/Y 1:1	5.2967	anti	H-bonded
EJEQIV	D	Luteolin	1:1	$P\,2_1$	Z	5.8084	para	H-bonded
EJEQOB	D	Chrysin	1:1	$P\,2_1\,2_1\,2_1$	C	5.2885	para	non-H-bonded
EJEQUH	D	Genistein	1:2	P 1	Y	5.3009	anti	H-bonded
EJERAO	D	Quercetin	1:2	$P\,2_1$	C/Y 1:1	5.4237	anti	H-bonded
EJERES	L	Quercetin	1:2	$P\,2_1$	C/Y 1:1	5.4354	anti	H-bonded
EJERIW	L	Kaempferol	1:2	$P\,2_1$	Y	5.36	anti	H-bonded
FEVZOX	D	S-Naproxen	1:1	$P\,2_1$	Z	5.7713	anti	H-bonded
FEVZUD	L	S-Naproxen	1:1	$P\,2_1$	Y	5.6999	anti	H-bonded
GIHSOH	L	Fumaric acid	1:2	$P\,2_1$	other	6.589	para	H-bonded
GIHSUN	D	Fumaric acid	1:2	$P\,2_1$	other	6.589	para	H-bonded
GIVROS	L	(11R,12R)-(+)-9,10-Dihydro-9,10-ethanoanthracene-11,12-dicarboxylic acid	1:1	$P\,2_1\,2_1\,2_1$	other	8.436	isolated	-
IHUMAZ	L	1,1-Dicyano-2-(4-hydroxyphenyl) ethene	2:2	$P\,2_1$	C/Y 1:1	5.2827	para	non-H-bonded
JOKLEC	L	1,1'-binaphthalene-2,2',7,7'-tetrol	1:1	$P\,2_1\,2_1\,2$	other	10.1763	anti	non-H-bonded
KECJIM	L	4-ethoxyphenylboronic acid	2:2	P 1	other	7.3764	para	non-H-bonded
KEFWAW	L	Ezetimibe	1:1	$P\,2_1$	Y	5.79905	para	H-bonded
LOXCOS	L	1,4-phenylenediboronic acid	1:2	P 1	dimer	-	-	-
LOXDIN	L	Phenylboronic acid hydrate	1:1:1	$P\,2_1$	Z	5.8462	para	non-H-bonded
LOXHAJ	L	(4-iodophenyl)boronic acid	1:1	$P\,2_1$	Z	6.5850	anti	non-H-bonded
LOXHAJ01	L	(4-iodophenyl)boronic acid	1:1	$P\,2_1\,2_1\,2_1$	Z	6.5921	anti	non-H-bonded

LOXHIR	L	Phenylboronic acid	1:1	P 2_1	other	9.055	para	non-H-bonded
NAZGIG	L	(2S,3R,4R,5S,6R)-2-(3-(4-Ethylbenzyl)-phenyl)-6-hydroxy-methyl-tetrahydro-2H-pyran-3,4,5-triol hydrate	1:2:4	P 2_1	Y/Z 1:1	5.7569	anti	non-H-bonded
NAZGOM	L	(2S,3R,4R,5S,6R)-2-(3-(4-Ethylbenzyl)-phenyl)-6-hydroxy-methyl-tetrahydro-2H-pyran-3,4,5-triol ethanol solvate hydrate	1:2:1:1	P 1	Y/Z 1:1	5.7299	anti	non-H-bonded
NAZGUS	L	(2S,3R,4R,5S,6R)-2-(3-(4-Ethylbenzyl)-phenyl)-6-hydroxy-methyl-tetrahydro-2H-pyran-3,4,5-triol	1:1	P 2_1 2_1 2_1	Z	5.75	isolated	
NAZHAZ	L	(2S,3R,4R,5S,6R)-2-(3-(4-Ethylbenzyl)-phenyl)-6-hydroxy-methyl-tetrahydro-2H-pyran-3,4,5-triol	2:4	P 1	Z	5.712	anti	non-H-bonded
NISVOA01	L	(S)-1,1'-binaphthalene-2,2'-diol	2:1	P 2_1 2_1 2_1	other	9.0398	isolated	-
PEBZOO	L	Resveratrol	1:1	P 2_1	other	6.6519	para	non-H-bonded
PEBZUU	L	Resveratrol	1:2	P 2_1 2_1 2_1	Y	5.5674	para	H-bonded
POKHAY10	L	4-(2,4,6-Tri-isopropyl-benzoyl)benzoic acid	2:2	P 2_1	Z	5.825	anti	non-H-bonded
PROLIN03	L	-	-	P 2_1 2_1 2_1	Y	5.28018	anti	H-bonded
PROLIN04	L	-	-	P 1	Y	5.21242	anti	H-bonded
QIRNUC	L	4-nitrophenol	2:1	P 2_1 2_1 2_1	Z	5.9045	isolated	-
RUWGEV	L	Hydrate	1:1	C 2	C	5.136	anti	H-bonded
TUGWAV	L	(Calixarene) CF_3CH_2OH solvate	2:2:5.2	P 1	isolated	-	-	-
UFOQEN	L	Thiourea hydrate	1:1:1	P 2_1 2_1 2_1	Z	5.7689	para	non-H-bonded
VESCUS	L	Pentacyclo(5.3.0.$0^{2,5}$.$0^{3,9}$.$0^{4,8}$)decane-2,5-dicarboxylic acid	1:1	P 2_1	other	8.028	para	non-H-bonded
VEVKEP	L	R-flurbiprofen	2:2	P 1	C	5.81938	anti	non-H-bonded
VEVKEP01	L	R-flurbiprofen	2:2	P 2_1	Z	5.8702	para	non-H-bonded
VEVKOZ	L	R-flurbiprofen	2:1	P 2_1	Z	5.7851	para	non-H-bonded
VEVKUF	L	R-flurbiprofen	1:3	P 2_1 2_1 2_1	C/Y/Z 1:1:1	5.6866	anti	H-bonded
VEVLAM	L	R-flurbiprofen	1:2	P 2_1	Z	5.99344	cross	H-bonded
VEVLEQ	L	R-flurbiprofen methanol solvate	1:1:0.5	C 2	Z	6.142	cross	H-bonded
VEVLEQ01	L	R-flurbiprofen methanol solvate	1:1:0.5	C 2	Z	6.044	cross	H-bonded
VEVLOA	L	R-flurbiprofen ethanol solvate	1:1:0.5	C 2	Z	6.187	cross	H-bonded
VEVLUG	D	R-flurbiprofen	2:1	P 2_1	Z	5.9554	para	non-H-bonded
VEVMAN	D	R-flurbiprofen	2:2	I 2	Z	5.7902	para	H-bonded
VEVMOB	D	rac-flurbiprofen	2:2	P 2_1	Z	5.7912	anti	non-H-bonded
VEVMOB01	D	rac-flurbiprofen	2:2	P 2_1	Z	5.91137	anti	non-H-bonded
VEVMUH	L	rac-flurbiprofen	2:2	P 1	Y/Z 1:1	5.76337	para	H-bonded
VEVMUH01	L	rac-flurbiprofen	2:2	P 1	Y	5.6856	anti	H-bonded
VEVNIW	L	rac-flurbiprofen	2:1	P 1	Z	5.8399	para	non-H-bonded
XEGKIG	L	2,4-dichlorobenzoic acid hydrate	4:2:1	P 1	non-HB	-	-	-
YEPJEL	L	Riluzole	1:1	P 2_1	Y	5.425	para	H-bonded
ZAPDAY	L	Benzoic acid	1:1	P 2_1 2_1 2_1	Z	5.6993	para	H-bonded
ZEZHIV	L	2,5-dihydroxybenzoic acid	1:1	P 2_1 2_1 2_1	Z	5.896	para	H-bonded

a) The number of molecules of API, proline and solvent(s) in the asymmetric unit.

b) For description of main chain types, see Scheme S2. “Other” stands for unclassified hydrogen-bonded chains that differ from presented in Scheme S2. “non-HB” corresponds to the **Pro** chain held only by close contacts, while “isolated” denotes the structure where individual molecules of proline are separated by other molecules. In cases where different symmetry-independent Pro zwitterions form different types of chains, the ratio between them is given.
c) The difference between “*para*” and “*anti*” double chains is shown in Scheme S3. “Cross” stands for the structure where the nearest **Pro** chains are not collinear. In ”isolated” structures, the chains are separated from each other by other molecules.
d) For difference between H-bonded and non-H-bonded, see Scheme S3 and Section 3.1 of the main text.
e) Structures from the present work

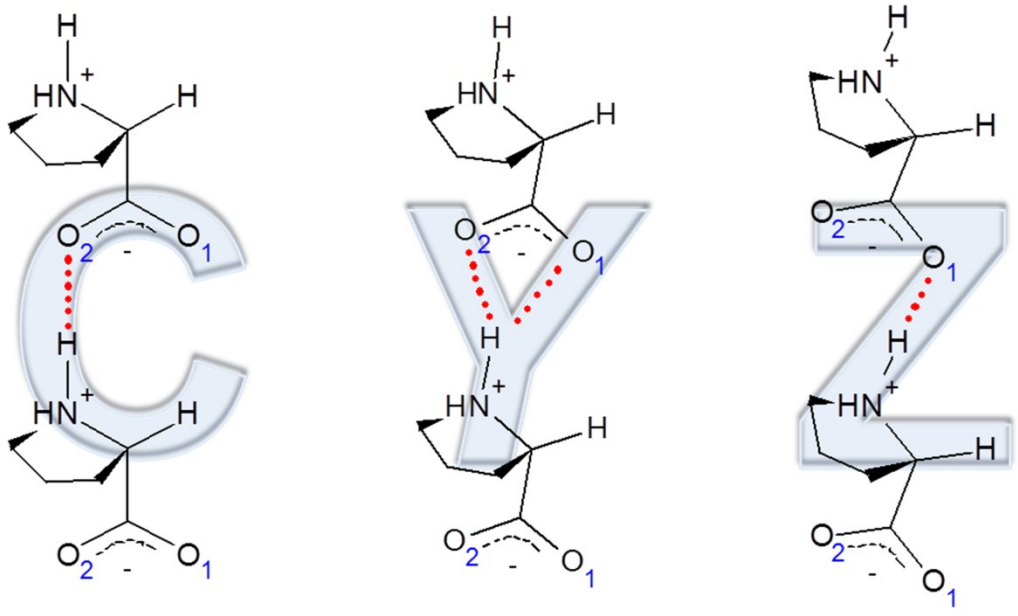

(a) (b) (c)

Scheme S2. A schematic image of the hydrogen-bonded chain motifs of proline zwitterions found in cocrystals with fenamates named C-type (a), Y-type (b) and Z-type (c).

The XPac analysis allowed us to elucidate that the main packing motifs in the crystals extracted from the CSD are the hydrogen-bonded chains of **Pro** formed in 64 of 68 crystals. Of them, the vast majority (52 structures) belongs to head-to-tail chains differing only by the acceptor atom of the $^{+}$N-H···O^{-} bond (shown in the Scheme S2 as O1 and O2) that we named Z-, Y- and C-chains (Scheme S2). In the C-type chain observed in [**Dic+Pro**] cocrystal as well as in the crystals of pure proline, the $^{+}$N-H···O^{-} bond is parallel, so that the synthon resembles the letter "C". The root-mean-square plane of the cyclic fragment of **Pro** within the C-chain is almost perpendicular to the chain direction. In the Z-chain, the $^{+}$N-H···O^{-} bond forms the angle close to 30° to the chain direction. An intermediate synthon type between C- and Z-chains, distinguished by a bifurcated H-bond with the common N-H donor, is named by us Y-chain. One needs to note, though, that the division of chain motifs into the Z-, Y- and C-types is not strict and reflects the extreme cases of the hydrogen-bonded group arrangement within the chain.

The chain structure from the [**CLX+Pro**] and [**NFA+Pro**] crystals (Z-chain) occurs in 32 proline crystals of 68 considered, or 47% of structures (Table S2). The chain type formed in the [Dic+Pro] (C-chain), is presented in 10 structures (15%). An intermediate Y-type chain is observed in 21 crystals (31%). A deeper analysis of the CSD data reveals the tendency of **Pro** to form mostly Z-chains in the cocrystals of 2:1 API:**Pro** ratio, and C- and Y-chains in crystals with the excess of Proline as well as in pure **Pro** and its hydrate.

In most structures, the H-bonded chains are oriented along one of crystallographic axes, which allows to estimate the chain period from the corresponding lattice parameter. The average value of

chain period is found to be 5.83 Å for the Z-type chain and 5.32 Å for the C-type chain, highlighting the difference between them. Note that in crystals of pure Pro and its hydrate only denser C-chains are formed.

Alternative rarer chain types not discussed in the present article which differ from the ones considered above are formed in crystals where the second component has two or more strong H-bond donors located close to each other, such as in cocrystals with phenylboronic acid derivatives and some other crystals (Table S2). Proline zwitterions are either arranged in a 'side-to-side' manner or their pattern is more complex than simple translation in Z-, Y- and C-chains. The oxygen atoms of Pro within these motifs are involved into the strong interactions with API molecules, leading to the formation of the 'side-to-side' motifs. In some of these crystals, one of the N-H groups of Pro is free and does not participate in any hydrogen bonding.

The tendency is studied in the Discussion section of the main paper.

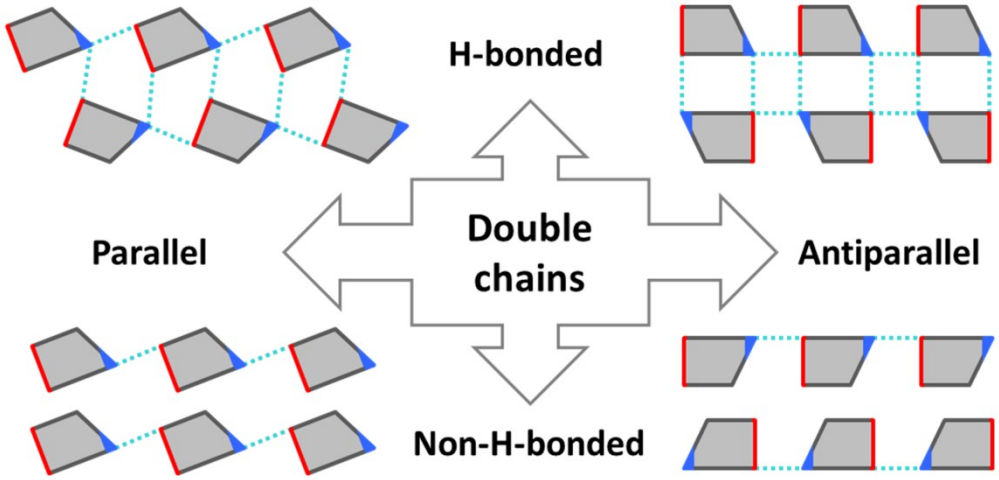

Scheme S3. Classification of double chain motifs of Proline zwitterions in crystals found in the CSD.

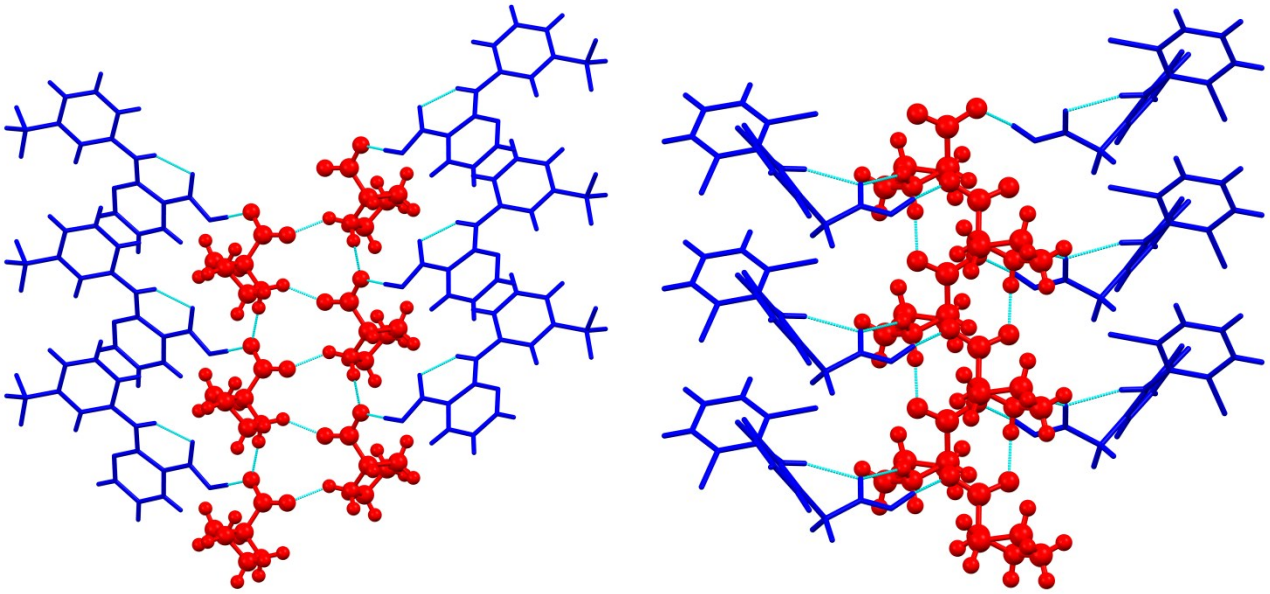

(a) (b)

Fig. S5. Images of hydrogen-bonded ribbons consisting of a proline double chain (coloured red) with API molecules (blue) attached by the strong O-H···O bond in the cocrystals: [**NFA**+**Pro**] (a); [**Dic**+**Pro**] (b).

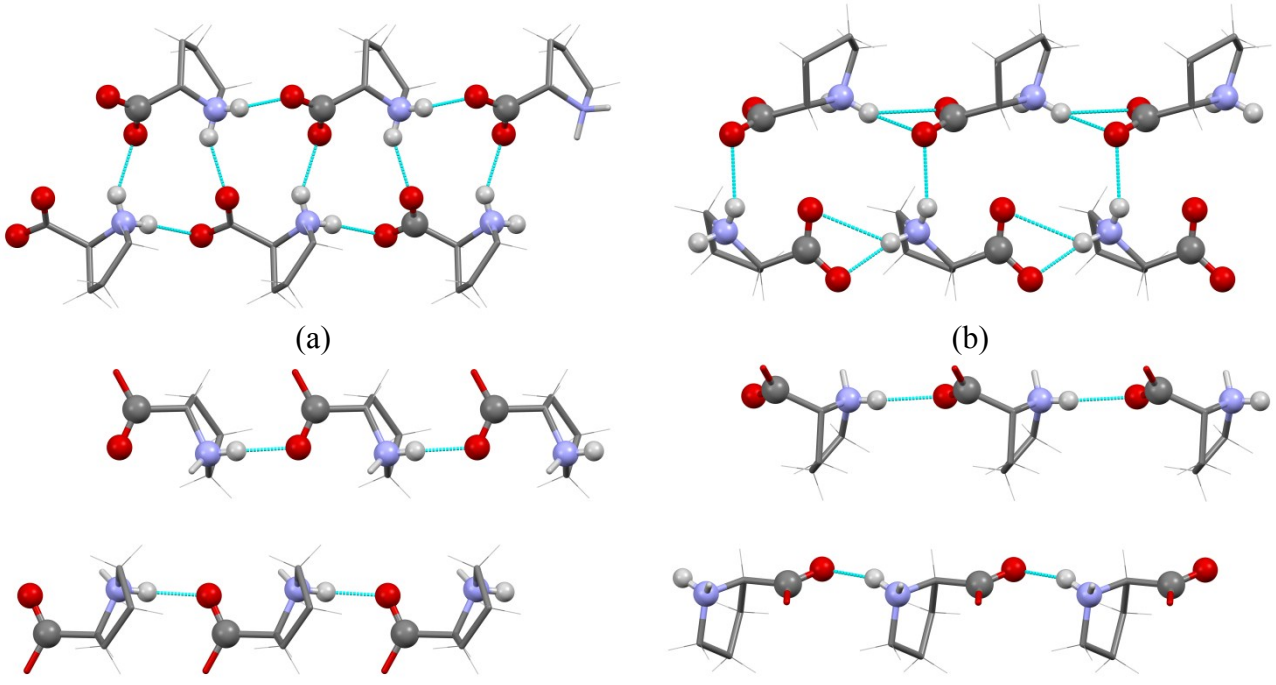

(a) (b)

(c) (d)

Fig. S6. Examples of double chain motifs observed in the structures from the CSD with different type of inter-chain bonding and mutual orientation: parallel H-bonded (EJEPUG, Z-chains) (a); antiparallel H-bonded (FEVZUD, Y-chains) (b); parallel non-H-bonded (EJEQAN, C-chains) (c); antiparallel non-H-bonded (VEVMOB, Z-chains) (d).

3.3 Pattern of non-covalent interactions in cocrystals

Table S3. Metric parameters and electron-density features at the (3;-1) bond critical points corresponding to noncovalent interactions[a] in the [**Dic+Pro**] (1:1) cocrystal. The numeration in the table is consistent with the .cif file.

Interaction	D(D···A)/ Å | D(H···A)/ Å	∠(D-H-A)/ °	ρ_b/ a.u.	$\nabla^2\rho_b$/ a.u.	G_b/ a.u.	E_{int}/ kJ·mol^{-1}
O2-H2···O4[a]	2.536 | 1.499	178.05	0.076	0.155	0.055	62.3
N2-H22···O3[b]	2.660 | 1.628	164.09	0.057	0.152	0.042	47.6
N1-H1···O1[c]	2.847 | 1.901	152.63	0.030	0.086	0.022	25.3[b]
N2-H21···O1[d]	2.816 | 1.972	137.03	0.025	0.077	0.019	21.7
C33-H33···O3[e]	3.395 | 2.443	145.12	0.011	0.035	0.008	9.0
C31-H31B···O2[f]	3.542 | 2.469	166.77	0.010	0.030	0.007	7.9
C33-H33···O4[b]	3.217 | 2.594	115.44	0.009	0.031	0.007	7.5
O4···N2[e]	3.066	-	0.008	0.032	0.007	7.5
C17-H18···Cl2[b]	3.664 | 2.790	136.66	0.008	0.029	0.006	6.6
C32-H32B···O4[e]	3.439 | 2.685	125.47	0.007	0.025	0.005	5.9
C30-H30A···Cl2[d]	3.801 | 2.810	151.16	0.007	0.026	0.005	5.7
C24-H24···C23[d]	3.650 | 2.661	151.36	0.008	0.024	0.005	5.6
Cl1···Cl1[g]	3.475	-	0.006	0.025	0.005	5.3
C32-H32A···O2[h]	3.382 | 2.713	119.13	0.006	0.023	0.005	5.2
H25···H14[i]	2.282	-	0.007	0.023	0.004	5.1
C17-H17···C12[b]	3.288 | 2.903	100.88	0.007	0.023	0.004	5.0
C12-H12···Cl1[f]	3.573 | 2.932	118.12	0.006	0.023	0.004	4.9
C13-H13···C25[j]	3.558 | 2.770	129.37	0.006	0.022	0.004	4.7
C14-H14···C26[j]	3.701 | 2.793	141.08	0.006	0.020	0.004	4.6
Cl2···O3[k]	3.344	-	0.005	0.020	0.004	4.5
Cl2···O1[l]	3.487	-	0.005	0.019	0.004	4.2
C30-H30B···Cl2[k]	3.663 | 2.984	120.61	0.005	0.019	0.004	4.1
C17-H18···N1[b]	3.773 | 2.796	129.93	0.005	0.017	0.004	4.0
H32A···H32B[m]	2.356	-	0.005	0.018	0.003	3.9
C24···Cl1[l]	3.539	-	0.006	0.017	0.003	3.8
C15-H15···C30[g]	3.631 | 2.985	118.41	0.004	0.016	0.003	3.2
C23-H23···C13[f]	3.867 | 3.059	131.71	0.004	0.012	0.002	2.6
C13···C15[l]	3.652	-	0.003	0.010	0.002	2.3
					E_{coh}/ kJ·mol^{-1}	**254.9**

[a] Distance between the donor and acceptor atoms D(D···A) and between the hydrogen and acceptor atom D(H···A), where D= O, N, C and A= O, N, C, angle ∠(D-H-A), electron density in bond CP $\rho_{b,}$ Laplacian of electron density in bond CP $\nabla^2\rho_b$, local kinetic energy in bond CP G_b, energy of intermolecular interaction E_{int} obtained using eq. (s4). All the solid-state calculations are performed at the B3LYP-D2/6-31G(d,p) level of theory.

[b] The intramolecular contacts are not taken into account in the E_{coh} evaluation.

Symmetry codes: a) x,-1+y,-1+z; b) x,-1+y,z; c) x,y,z; d) -x,1/2+y,-z; e) -x,-1/2+y,1-z; f) 1-x,1/2+y,-z; g) 1-x,-1/2+y,-z; h) x,1+y,1+z; i) -1+x,1+y,z; j) 1+x,y,z; k) -x,-1/2+y,-z; l) x,1+y,z; m) 1-x,-1/2+y,1-z.

Table S4. Metric parameters and electron-density features at the (3;-1) bond critical points corresponding to the noncovalent interactions[a] in the [**CLX+Pro**] (1:1) cocrystal. The numeration in the table is consistent with the .cif file.

Interaction	D(D···A)/ Å | D(H···A)/ Å	∠(D-H-A)/ °	ρ_b/ a.u.	$\nabla^2\rho_b$/ a.u.	G_b/ a.u.	E_{int}/ kJ·mol^{-1}
O11-H11···O1[a]	2.558 | 1.545	174.13	0.065	0.166	0.049	55.6
N1+-H1···O1[b]	1.648 | 2.689	169.14	0.053	0.147	0.040	44.8
N12-H12···O12[c]	2.700 | 1.823	142.05	0.037	0.113	0.029	32.6[b]
N1+-H2···O2[d]	2.774 | 1.844	147.51	0.032	0.099	0.025	27.7
C26-H26···N11[c]	2.897 | 2.181	121.79	0.022	0.070	0.016	18.3[b]
N12-H12···C27[c]	2.823 | 2.363	106.30	0.015	0.069	0.014	15.6[b]
C27-H271···Cl1[c]	3.127 | 2.618	107.66	0.013	0.055	0.011	12.5[b]
C15-H15···O2[b]	3.292 | 2.322	147.47	0.013	0.039	0.009	10.7
C14-H14···O1[e]	3.358 | 2.377	149.85	0.012	0.037	0.009	10.0
C5-H52···N11[c]	3.485 | 2.522	146.67	0.010	0.030	0.007	7.7
C27-H273···O11[f]	3.482 | 2.581	139.11	0.009	0.031	0.007	7.5
C13-H13···O11[g]	3.430 | 2.627	130.38	0.007	0.027	0.006	6.5
C3-H31···O12[h]	3.418 | 2.597	131.16	0.007	0.026	0.006	6.3
C4-H41···C23[i]	3.691 | 2.683	153.36	0.008	0.025	0.005	5.6
C2-H21···C14[j]	3.474 | 2.698	127.64	0.008	0.024	0.005	5.5
C25-H25···Cl1[k]	3.649 | 2.815	133.58	0.006	0.025	0.005	5.4
H25···H272[i]	2.248	-	0.007	0.025	0.005	5.4
C2-H21···O12[h]	3.489 | 2.783	122.22	0.005	0.020	0.004	4.5
Cl1···N12[f]	3.603	-	0.005	0.016	0.003	3.7
H25···H42[c]	2.532	-	0.005	0.018	0.003	3.7
C13··· N12[b]	3.441	-	0.005	0.015	0.003	3.7
C14···C21[b]	3.479	-	0.005	0.016	0.003	3.6
C5-H51···Cl1[i]	3.868 | 3.121	126.21	0.005	0.015	0.003	3.2
C4-H42···Cl1[k]	3.686 | 3.147	111.13	0.004	0.015	0.003	3.1
C3-H32···C27[h]	3.794 | 3.170	117.06	0.003	0.011	0.002	2.3
C3-H31···C24[i]	3.863 | 3.163	122.47	0.003	0.010	0.002	2.1
					E_{coh}/ kJ·mol^{-1}	**213.7**

[a)] Distance between the donor and acceptor atoms D(D···A) and between the hydrogen and acceptor atom D(H···A), where D= O, N, C and A= O, N, C, angle ∠(D-H-A), electron density in bond CP $\rho_{b,}$ Laplacian of electron density in bond CP $\nabla^2\rho_b$, local kinetic energy in bond CP G_b, energy of intermolecular interaction E_{int} obtained using eq. (s4). All the solid-state calculations are performed at the B3LYP-D2/6-31G(d,p) level of theory.

[b)] The intramolecular contacts are not taken into account in the E_{coh} evaluation.

Symmetry codes: a) 1+x,-1+y,z; b) 1+x,y,z; c) x,y,z; d) 1/2+x,1/2-y,1-z; e) 1.5+x,1/2-y,1-z; f) -1+x,y,z; g) 1/2+x,-1/2-y,1-z; h) x,1+y,z; i) -x,1/2+y,1/2-z; j) -1/2+x,1/2-y,1-z; k) -1-x,1/2+y,1/2-z.

Table S5. Metric parameters and electron-density features at the (3;-1) bond critical points corresponding to the noncovalent interactions[a] in the [**NFA+Pro**] (1:1) cocrystal. The numeration in the table is consistent with the .cif file.

Interaction	D(D···A)/ Å | D(H···A)/ Å	∠(D-H-A)/ °	ρ_b/ a.u.	$\nabla^2\rho_b$/ a.u.	G_b/ a.u.	E_{int}/ kJ·mol^{-1}
O1-H1···O3[a]	2.559 | 1.541	174.85	0.066	0.162	0.050	56.0
N3-H31···O3[b]	2.721 | 1.685	167.99	0.049	0.136	0.036	40.3
N1-H11···O2[c]	2.700 | 1.847	138.81	0.035	0.107	0.027	30.9[b]
N3-H32···O4[d]	2.832 | 1.924	144.32	0.026	0.081	0.020	22.9
N3···O4[c]	2.673	-	0.020	0.084	0.019	21.0[b]
C22-H22···N2[c]	2.940 | 2.327	114.30	0.016	0.057	0.012	13.9[b]
C14-H14···O3[e]	3.243 | 2.395	134.15	0.012	0.039	0.009	10.3
C31-H31B···O2[f]	3.310 | 2.442	135.34	0.010	0.034	0.008	8.5
C33-H33A···N2[c]	3.454 | 2.453	151.97	0.011	0.033	0.008	8.5
C13-H13···O4[b]	3.209 | 2.503	121.62	0.009	0.033	0.007	8.2
C31-H31A···F3[g]	3.479 | 2.475	154.08	0.008	0.032	0.007	7.7
C31-H31B···F3[h]	3.407 | 2.634	127.13	0.007	0.032	0.007	7.4
F1···F2[h]	2.891	-	0.005	0.032	0.007	7.3
C32-H32B···F2[c]	3.309 | 2.560	124.97	0.006	0.030	0.006	6.7
C25-H25···C25[i]	3.708 | 2.690	156.12	0.008	0.025	0.005	5.8
C33-H33B···F3[h]	3.407 | 2.634	127.13	0.005	0.026	0.005	5.7
C32-H32B···F2[h]	3.608 | 2.631	148.58	0.005	0.024	0.005	5.3
C30-H30A···O2[f]	3.404 | 2.733	119.42	0.006	0.022	0.005	5.1
C15-H15···O1[j]	3.687 | 2.683	153.86	0.006	0.021	0.005	5.1
C26-H26···C11[j]	3.366 | 2.839	109.81	0.007	0.023	0.004	5.0
C32-H32B···F1[g]	3.254 | 2.750	107.78	0.005	0.023	0.004	4.8
C31-H31A···F1[g]	3.312 | 2.806	108.12	0.004	0.022	0.004	4.7
C32-H32B···F3[g]	3.330 | 2.879	104.84	0.004	0.021	0.004	4.4
C30-H30A···C15[k]	3.707 | 2.779	142.74	0.006	0.020	0.004	4.3
H13···H32A[b]	2.342	-	0.005	0.017	0.003	3.7
C15···N1[b]	3.556	-	0.004	0.013	0.003	3.0
C22-H22···C25[b]	3.747 | 3.258	108.74	0.003	0.010	0.002	2.1
					E_{coh}/ kJ·mol^{-1}	**242.9**

[a)] Distance between the donor and acceptor atoms D(D···A) and between the hydrogen and acceptor atom D(H···A), where D= O, N, C and A= O, N, C, angle ∠(D-H-A), electron density in bond CP ρ_b, Laplacian of electron density in bond CP $\nabla^2\rho_b$, local kinetic energy in bond CP G_b, energy of intermolecular interaction E_{int} obtained using eq. (s4). All the solid-state calculations are performed at the B3LYP-D2/6-31G(d,p) level of theory.

[b)] The intramolecular contacts are not taken into account in the E_{coh} evaluation.

Symmetry codes: a) 1+x,-1+y,z; b) x,-1+y,z; c) x,y,z; d) -x,-1/2+y,-z; e) -x,-1.5+y,-z; f) -1+x,y,z; g) -x,1/2+y,1-z; h) -x,-1/2+y,1-z; i) 1-x,1/2+y,1-z; j) 1-x,-1/2+y,-z; j) x,1+y,z; k) -x,1/2+y,-z.

Table S6. The comparison of energies of the heterosynthons formed by the O11-H11···O1$^-$ API-Pro hydrogen bond[a] in studied cocrystals and corresponding H-bonded homosynthons in crystals of pure APIs estimated by QTAIMC. The units are kJ·mol^{-1}.

Crystal	Dic	CLX	NFA
[API+Pro]	62.3	55.6	56.0
Pure API	40.7	39.3	37.2

[a)] The numeration of atoms corresponds to Fig. 3 and Table 2 in the main text.

S3.4. IR-spectroscopic study

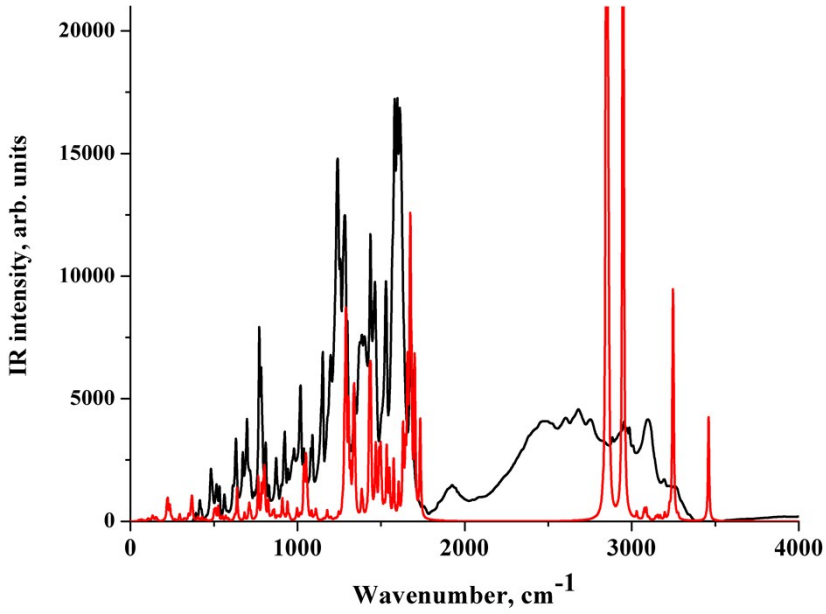

Fig. S7. Experimental (black) and theoretical (red) FTIR spectra of crystalline [**CLX+Pro**].

The theoretical spectrum of crystalline [**CLX+Pro**] is very close to the experimental one in the frequency region below 1800 cm^{-1} (Fig. S7). Differences between the calculated and experimental spectra in the region above 2000 cm^{-1} are due to mechanical and electro optical anharmonicity (see Section 2.4 of the main text). A tentative assignment of the band in the experimental spectrum is given in Table S7.

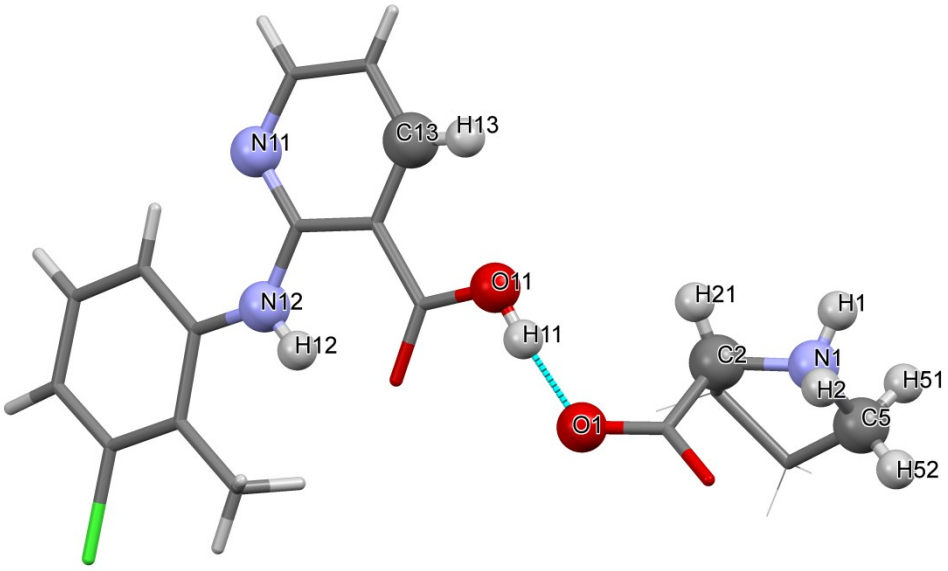

Fig. S8. The fragment of the [**CLX+Pro**] crystal with atom numbering.

Table S7. Comparison of the maxima of the absorption bands (cm^{-1}) in the IR spectrum of the [**CLX+Pro**] crystal, obtained experimentally (Exp.) and theoretically (Calc.). The numbering of atoms shown in Fig. S8 corresponds to the cif file of the [**CLX+Pro**] crystal.

Exp. [b]	Calc. [c]	Tentative assignment[d]
3310 w.	3325 (1135)	ν(N12-H)
3096 m.	3120 (2300) [e]	Antisymmetric vibration of the $^{+}$N1-H2···O2 fragment
2954 m.	2969 (112)	ν(C5-H)
2753 m.; 2680 m.	2836 (4787)	Antisymmetric vibration of the $^{+}$N1-H1···O1^{-} fragment and
2605 m.; 2476 m.	2733 (14042) [e]	antisymmetric vibration of the O11-H11···O1^{-} fragment
~ 1925 v.w.	1279+734	Combination σ(C13-H) +γ(N12-H)
1677 s.	1666 (767)	Deformation vibrations of secondary amines
1596 v.s.	1610 (3007) [e]	$\nu^{AS}(COO^{-})$ + γ(N1-H)
1437 v.s.	1474 (685)	Antisymmetric deformation vibration of the CH_3 group
1385 s.	1375 (1320)	$\nu^{S}(COO^{-})$ + γ(N1-H)
1284 v.s.	1279 (1008)	σ(C2-H)
1238 v.s.	1237 (2661)	σ(O11-H) + σ(C13-H)
1017 s.	994 (327)	CH_2 twisting
924 m.	-	γ(C-H)
771 s.	734 (412)	γ(N12-H)
698 m.	-	CH_2 rocking

[a] The calculated harmonic frequencies have been scaled by 0.9613 in accord with the Ref. [26]; [b] abbreviations used for relative intensities: vs, very strong; s, strong; m, medium; w, weak; vw, very weak; [c] IR intensities (kM/mol) are given in parentheses; [d] ν, σ and γ denote stretching, in-plane bending and out-of-plane bending vibrations, respectively; [e] the most IR intensive band among the group of bands with close frequencies (±20 cm^{-1})

S3.5. Dissolution experiments

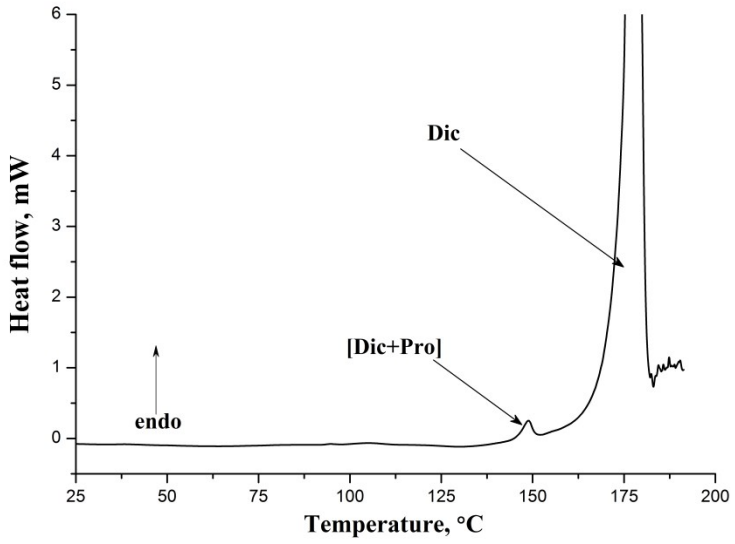

(a)

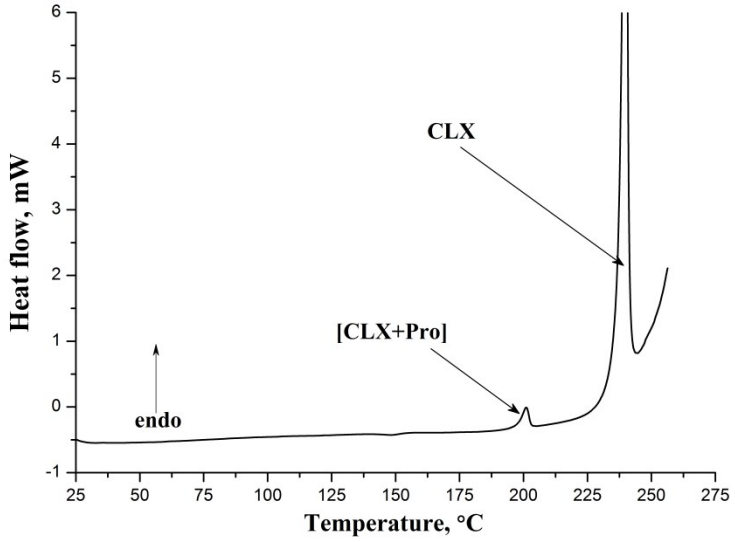

(b)

Fig. S9. Results of DSC analysis of the solid phases at the eutectic point for [**Dic+Pro**] (a) and [**CLX+Pro**] (b).

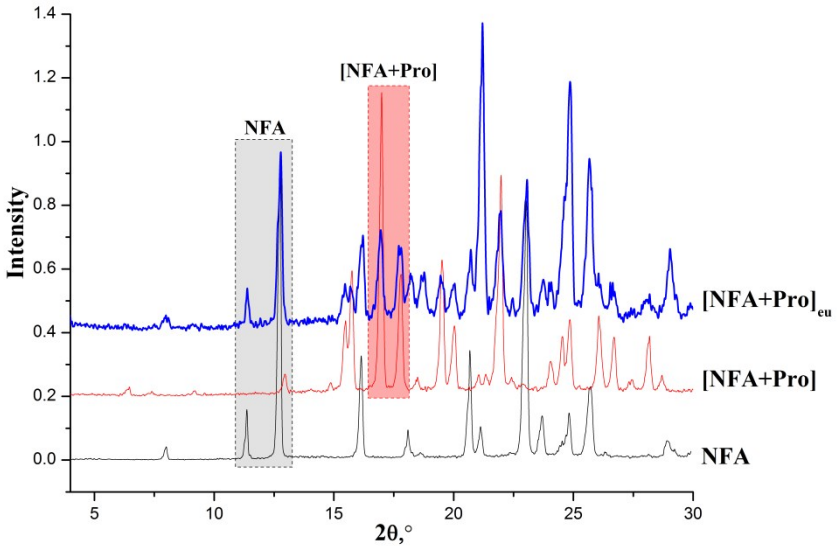

Fig. S10. PXRD patterns of **NFA**, [**NFA+Pro**] cocrystal and the solid phase at the eutectic point ([**NFA+Pro**]$_{eu}$)

S3.6. Details and outcome of competitive grinding experiment

In order to estimate the relative stability of obtained cocrystals, a competitive grinding experiment was conducted for ternary CLX-Dic-Pro, NFA-Dic-Pro and CLX-NFA-Pro systems. An equimolar (1:1:1) mixture of two fenamates and L-proline was placed into a milling jar and milled with 50 µl of ethanol for 60 min at 500 rpm. A subsequent PXRD analysis confirmed that the grinding of the three-component physical mixture consisting of **NFA/CLX**, **Dic** and **Pro** resulted in formation of the [**NFA+Pro**]/[**CLX+Pro**] cocrystal, while **Dic** remained unreacted (Figs. S11a,b). When the CLX-NFA-Pro mixture was ground, the cocrystal formation was observed only for [**NFA+Pro**] (Fig. S11c). Therefore, the relative stability of the cocrystals was found to increase in the following order: [**Dic+Pro**] < [**CLX+Pro**] < [**NFA+Pro**].

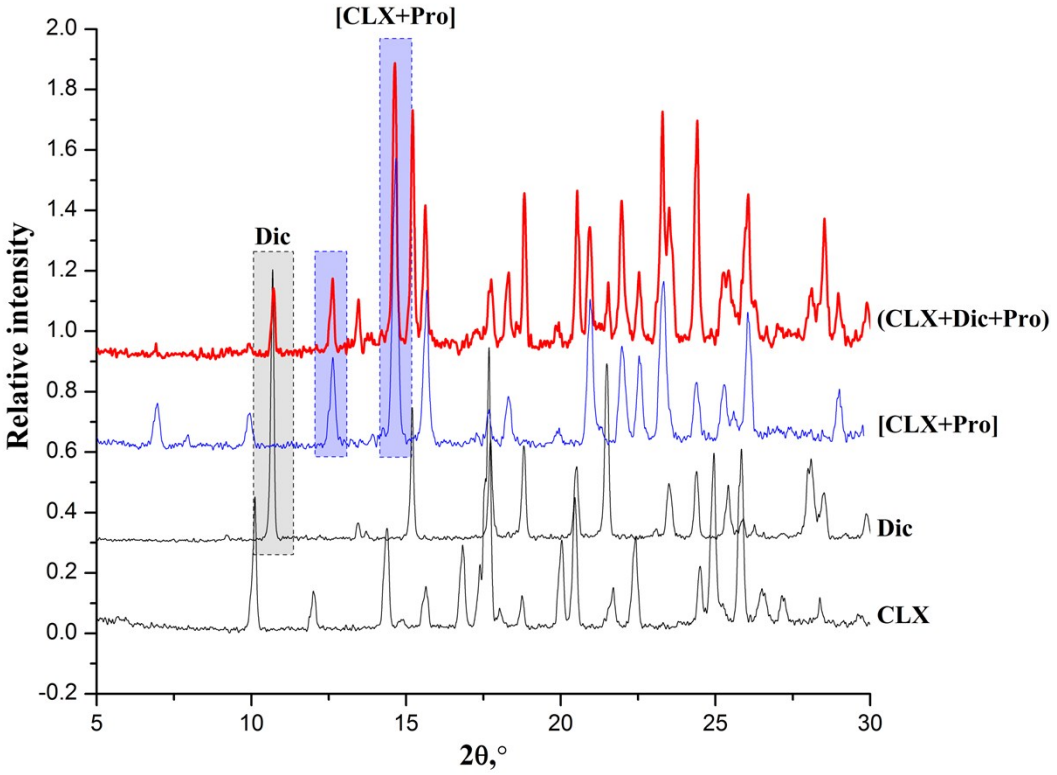
[CLX+Pro]
Dic
Relative intensity
(CLX+Dic+Pro)
[CLX+Pro]
Dic
CLX
2θ,°

(a)

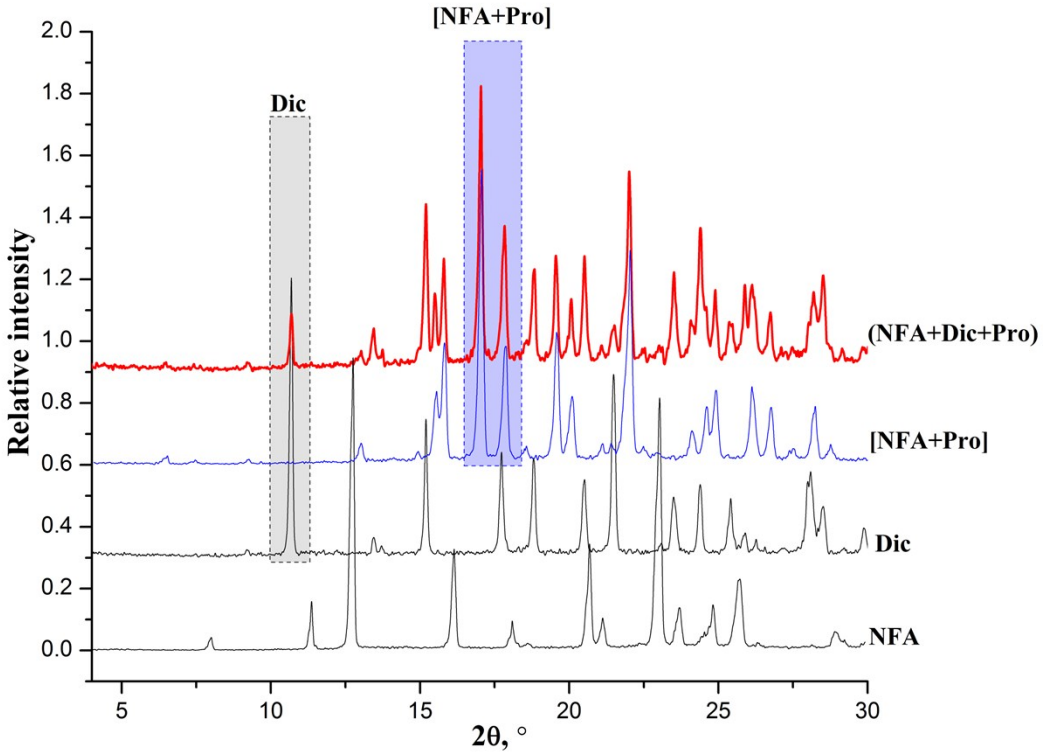
[NFA+Pro]
Dic
Relative intensity
(NFA+Dic+Pro)
[NFA+Pro]
Dic
NFA
2θ, °

(b)

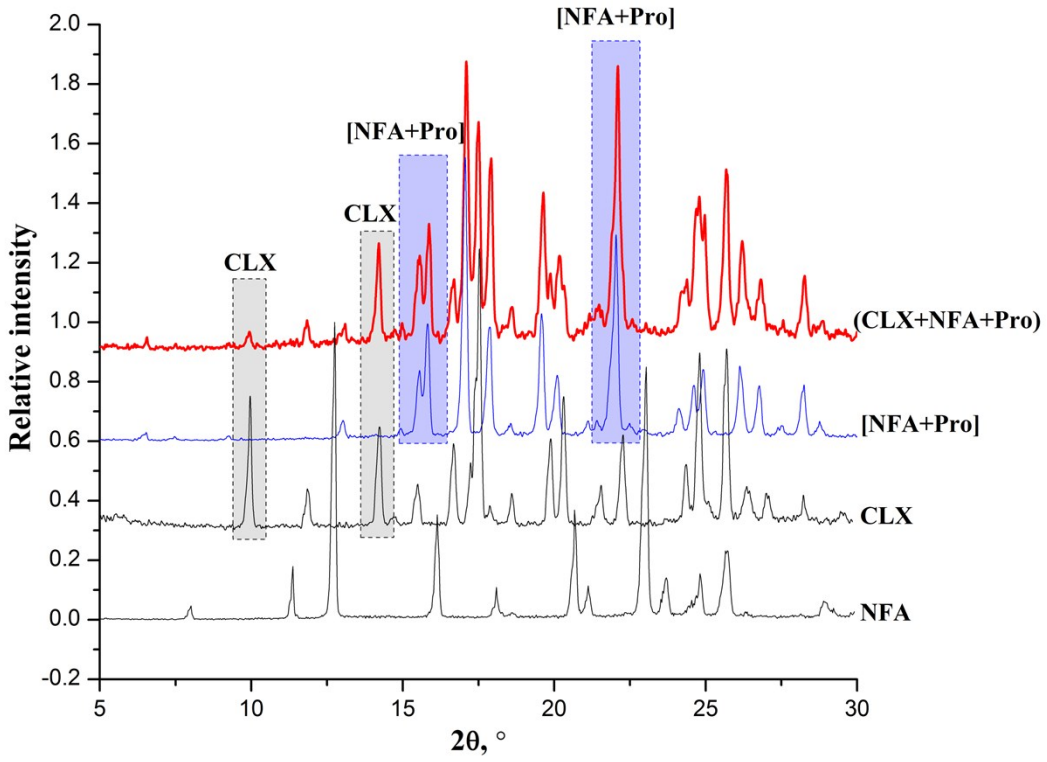

(c)

Fig. S11. Powder X-Ray diffraction patterns of samples after competitive grinding of equimolar mixtures: CLX + Dic + Pro (a); NFA + Dic + Pro (b); CLX + NFA + Pro (c). The shadowed areas correspond to the reflections in the sample common with the cocrystal (blue) or pure compound (grey)

S4. Discussion

S4.1. Analysis of supramolecular organisation features

Table S8. Types of double chain motifs observed in proline cocrystals with different stoichiometry. The graph set notations are given in parentheses [a)].

API:Pro ratio	H-bonded		Non-H-bonded		Other
	para	*anti*	*para*	*anti*	
2:1	-	-	VEVKOZ (*C*) VEVLUG (*C*) VEVNIW (*C*)	-	-
1:1	EJEPUG (*R*) EJEQIV (*R*) KEFWAW (*O*) VEVMAN (*R*) VEVMUH (*R*) YEPJEL (*O*) ZAPDAY (*R*) ZEZHIV (*O*) [**NFA+Pro**] (*R*) [**CLX+Pro**] (*R*)	FEVZOX (*D*) FEVZUD (*D*) VEVMUH01 (*R*)	EJEQAN (-) EJEQOB (-) IHUMAZ (-) KECJIM (*O*) LOXHIR (*C*) PEBZOO (*O*) VESCUS (*C*) VEVKEP01 (-) [**Dic+Pro**] (-)	JOKLEC (C) LOXHAJ (*C*) LOXHAJ01 (*C*) POKHAY10 (-) VEVKEP (-) VEVMOB(-) VEVMOB01(-)	-
1:2	GIHSOH (*R*) GIHSUN (*R*) PEBZUU (*O*)	BEJNAI (*O*) EJEPOA (*R*) EJEQER (-) EJEQUH (-) EJERAO (*O*) EJERES (*O*) EJERIW (*O*)	-	CIPVUU (*C*) NAZHAZ (*C*)	VEVLAM 90° chains (*R*)
1:3	-	VEVKUF (*R*)	-	-	-

[a)] "*R*" denotes $R^3_3(11)$; D^B; D^B; "*C*" stands for $C^1_1(5)$; D; D^B; "*D*" denotes D; D; D^B; "*O*" stands for other types of bifurcate oxygen; "-" denotes no bifurcate oxygen.

A more detailed analysis of data in Table S2 allowed us to yield some correlations concerning the supramolecular organisation which may be useful in the crystal engineering of proline zwitterionic cocrystals. For instance, it was found that antiparallel H-bonded double chains (Fig. S6b) are built almost exclusively from Y-type chains (Scheme S2) (9 of 11 structures). We have also noticed that all structures where Pro chains are isolated by API molecules crystallise into the $P2_12_12_1$ space group.

Despite the fact that there is only scarce data on the thermal properties of the proline cocrystals, we have managed to obtain the correlation linking the difference of melting points of an API (T_{fus}(API)) and an 1:1 API:Pro cocrystal (T_{fus}(CC)) with packing arrangement of the double chains. All points below the blue dotted line in the Fig. S12 correspond to API-Pro systems where T_{fus}(API) > T_{fus}(CC). It was found that almost all cocrystals with the parallel orientation of proline chains have melting point lower than their corresponding APIs which can be attributed to the packing

influence of the second component, i.e. proline. We assume that higher stability of antiparallel organisation of proline chains (formed in both polymorphic modification of pure L-Pro, see Table S2) compared to parallel double chains is the factor that causes increase in melting point of Pro cocrystals compared to the initial APIs.

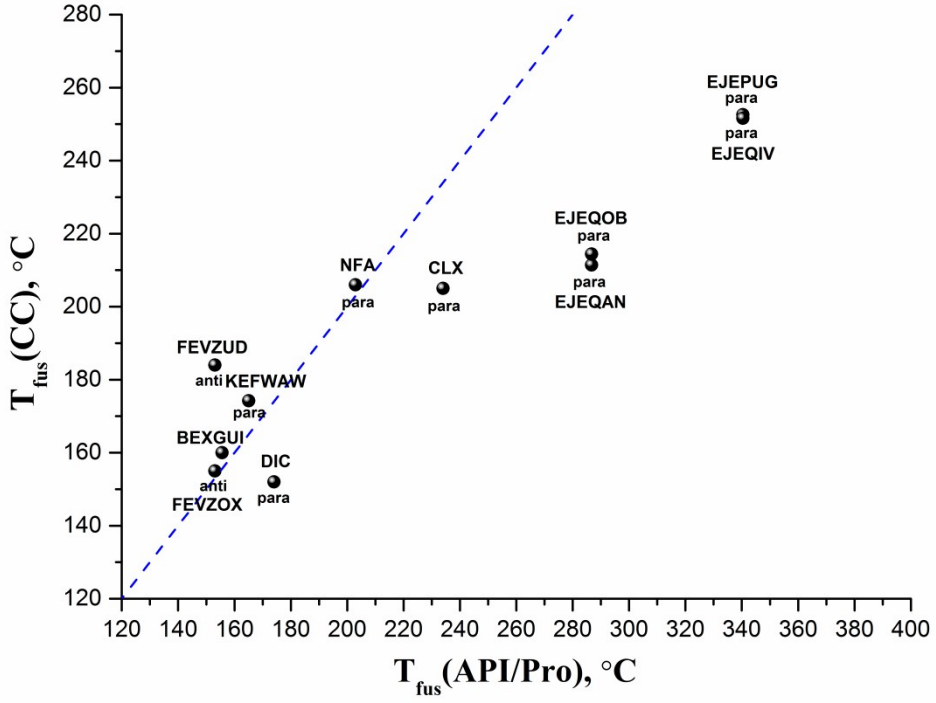

Fig. S12. The melting points of **Pro** cocrystals plotted against the melting points of their pure APIs. The blue dotted line corresponds to the bisector with T_{fus}(API) = T_{fus}(CC). The '*anti*' and '*para*' stand for parallel and antiparallel orientation of the proline chains. One can observe that all cocrystals with T_{fus}(CC) < T_{fus}(API) (points below the dotted line) have *para* double chains of **Pro** in their structure.

S4.2. Discussion on possible cooperativity effects in studied systems

According to the CSD survey results supported by the non-covalent interaction energy computations, the infinite hydrogen-bound chains are the main type of Long Range Aufbau Modules (a term proposed by Desiraju[27]) in pure amino acid crystals[28] and multicomponent crystals containing them. The prevailing interaction type, as shown in Refs. [29, 30] and confirmed in the present work using QTAIMC calculations, are the electrostatic forces. Hence, it is possible to consider the hydrogen-bonded **Pro** chains as chains of head-to-tail oriented dipoles. Charge-induced cooperative effect caused by the dipole-dipole interactions, was studied in Refs. [29, 31, 32]

Using the terminology of the cooperative effects we can explain the propensity of the proline chains to aggregation into larger supramolecular constructs. As demonstrated by the CSD survey, **Pro** tends to form double chains in most crystal structures with one of carboxylate oxygens accepting the intra-chain **H-**bond, and the other one accepting the inter-chain **H-**bond. Since the negative charge on the carboxylate ion is partially delocalised, the hydrogen bond at the oxygen atom O2 leads to an additional increase in the negative charge on the oxygen atom O1 and, therefore, is capable of amplifying the intra-chain bond. Similar effect, named 'resonance-assisted hydrogen bonding'[33] or π-cooperativity,[34] plays an important role in stabilising biological structures, such as pairs of complementary DNA bases[35] and protein secondary structures.[36] However, unlike crystals, the interaction of fragments within the biopolymer main chain occurs due to covalent, rather than hydrogen bonds.

In case when the inter-chain hydrogen bond between **Pro** zwitterions have a common acceptor (i.e. they are bifurcated), the mutual bond strengthening is expected. This non-additivity of H-bonding is known as polarisation-assisted hydrogen bonding[37] or σ-cooperative effect[34] in the literature. In a nutshell, this effect can be explained as an increase in the negative charge on the H-bond acceptor atom.

Obviously, the cooperative effects in proline cocrystals are not limited to **Pro**-**Pro** interactions. In fact, any strong H-bond between an API and the carboxylate group of **Pro** may additionally stabilise the proline double chain as presented in Fig. S13. Taking the above considerations into account, we suppose that cooperative effects may be at least partially responsible for the prevalence of the API-Pro ribbon structural motifs in proline cocrystals.

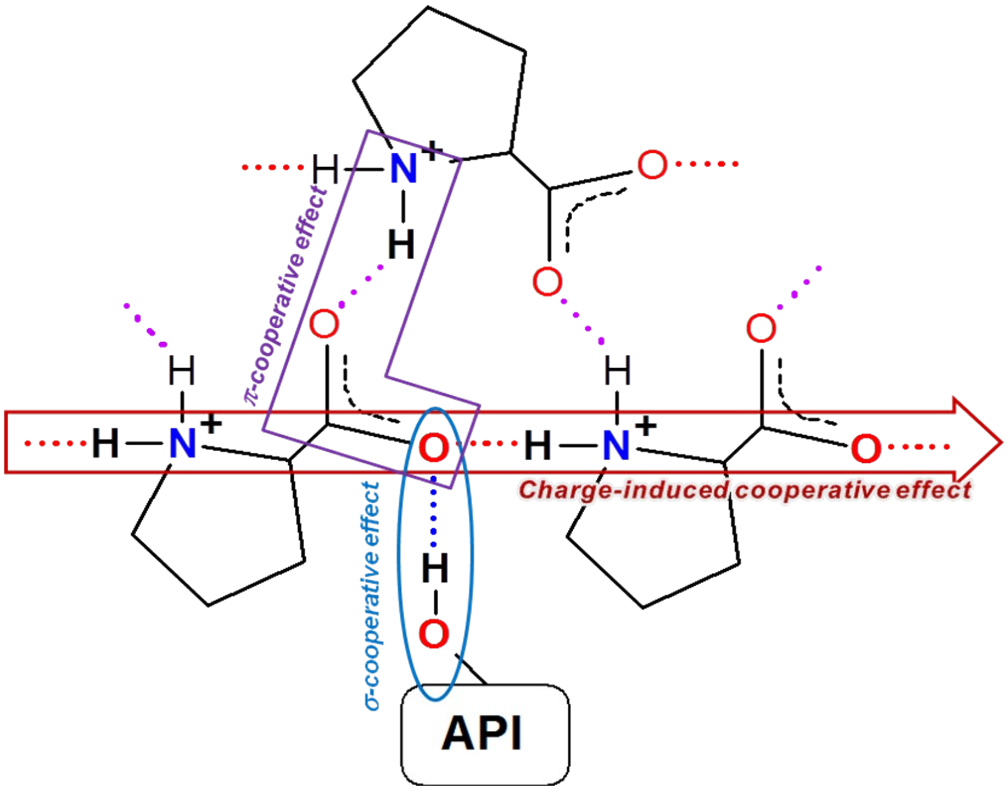

Fig. S13. Possible cooperative effects in hydrogen-bonded ribbons of proline with **CLX** and **NFA**.

S4.3. Modeling of the ribbon structures

The test modeling of the isolated **CLX-Pro** ribbon (Fig. 3 in the main text) extracted from the corresponding crystal has demonstrated that the structure of the hydrogen-bonded fragments for the system studied is almost unchanged in comparison with the crystal. The vibrational analysis performed on the optimised geometry confirmed that the structure is located in a local minimum on the potential energy surface. Due to the change in conformation of side aromatic fragments of **CLX**, the conformational energy change was calculated using the isolated **CLX** molecule in the relaxed conformation as a reference. In order to model the **TFA-Pro** ribbon, the clonixin molecule in the isolated **CLX-Pro** ribbon was replaced by tolfenamic acid extracted from the crystal of pure **TFA** Form I.

The metric and energetic properties of hydrogen bonds in the ribbons studied are listed in Table S9, and main contributions from different types of interactions are listed in Table S10. One can see that main structural and energetic properties of the ribbons with **TFA** and **CLX** are similar, despite the absence of a cocrystal in the **TFA-Pro** system. Further discussion on similarities and differences between the **CLX**-based and **TFA**-based ribbons is given in the Section 3.2 of the main text.

Total cohesive energy of the **CLX-Pro** ribbon estimated using QTAIMC equals to -207 kJ·mol^{-1} (Table S10), which equals about 70% of the E_{coh} value for the bulk crystal estimated by the same method (see the main text, Subsection 2.3), which confirms the primary role of interactions within the ribbon in the crystal lattice building. This value roughly corresponds to the contribution to the crystal cohesive energy from the noncovalent interactions within the ribbon motifs obtained from the solid-state DFT calculations.

Table S9. Calculated metric parameters, electron density in the (3, -1) critical point ρ_b, energies E_{HB} and enthalpies ΔH_{HB} of the hydrogen bonds in optimised ribbon motifs of L-proline with clonixin and tolfenamic acid.

Fragment	H-bond type	D(N···O), Å[a)] D(H···O), Å	∠(N-H-O), °	ρ_b, a.u.	-E_{HB},[b)] kJ·mol^{-1}
		[**CLX+Pro**]			
O11-H11···O1$^-$	API-Pro	2.613 | 1.611	174.96	0.053	46.3
N1$^+$-H1···O1$^-$	intra-chain	2.689 | 1.637	172.70	0.056	46.0
N1$^+$-H2···O4	inter-chain	2.717 | 1.746	153.98	0.040	35.2
		[**TFA+Pro**]			
O11-H11···O1$^-$	API-Pro	2.623 | 1.627	171.65	0.056	46.5
N1$^+$-H1···O1$^-$	intra-chain	2.684 | 1.632	172.13	0.051	44.3
N1$^+$-H2···O2	inter-chain	2.715 | 1.742	154.28	0.040	35.4

Table S10. The contributions from the interactions of different types into the cohesive energy of the optimised ribbon motifs of **CLX-Pro** and **TFA-Pro**[a] given in kJ·mol^{-1} and in % of the E_{coh}(ribbon) values. In the bottom row, the conformational energies of fenamates are given.

Structure	**CLX-Pro**	**TFA-Pro**
Conventional H-bonds	-127.5 (61.5%)	-126.2 (59.5%)
Non-conventional H-bonds	-49.0 (23.6%)	-49.5 (23.3%)
Other interactions	-31.0 (14.9%)	-36.1 (17.0%)
E_{coh} (ribbon), kJ·mol^{-1}	**-207.4**	**-212.0**
ΔE_{conf} (Fen)[b], kJ·mol^{-1}	5.9	15.5

[a] Estimated by equation (s4)

[b] ΔE_{conf} (Fen)= E(Fen)^{ribbon} – E(Fen)^{relaxed},
where E(Fen)^{ribbon} and E(Fen)^{relaxed} are total DFT-D2 energies of the fenamate molecule extracted from the ribbon and in the relaxed conformation, respectively.

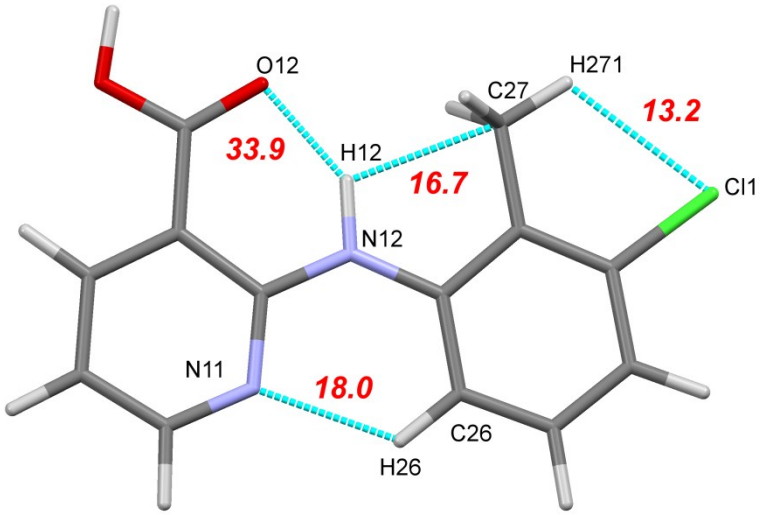

Fig. S14. Intramolecular contacts in **CLX** molecule in the optimised structure of the **CLX-Pro** ribbon. The numbers correspond to energies of particular interactions estimated by QTAIMC.

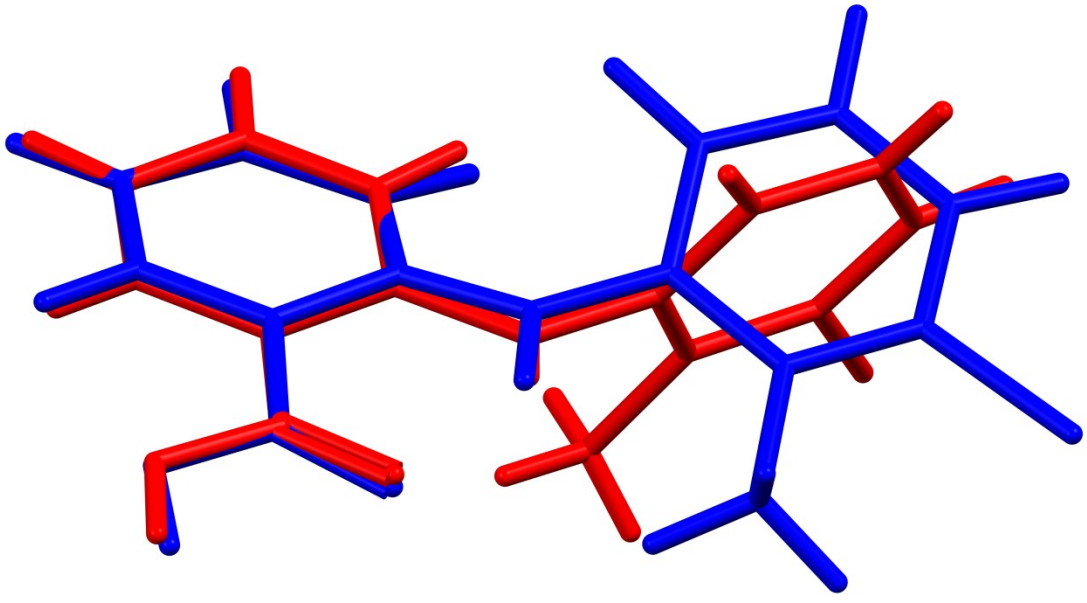

Fig. S15. Overlay of optimal **TFA** conformations within the ribbon (blue) and isolated molecule (red)

References

1. G. M. Sheldrick, *SADABS, Program for scaling and correction of area detector data*, University of Göttingen, Germany, 1997.
2. G. M. Sheldrick, *Acta Crystallographica Section A: Foundations of Crystallography*, 2008, **64**, 112-122.
3. D. J. Good and N. Rodriguez-Hornedo, *Crystal Growth & Design*, 2009, **9**, 2252-2264.
4. R. Dovesi, R. Orlando, A. Erba, C. M. Zicovich‐Wilson, B. Civalleri, S. Casassa, L. Maschio, M. Ferrabone, M. De La Pierre and P. D'Arco, *International Journal of Quantum Chemistry*, 2014, **114**, 1287-1317.
5. S. Grimme, *Journal of computational chemistry*, 2006, **27**, 1787-1799.
6. S. Grimme, J. Antony, S. Ehrlich and H. Krieg, *The Journal of chemical physics*, 2010, **132**, 154104.
7. S. Grimme, S. Ehrlich and L. Goerigk, *Journal of computational chemistry*, 2011, **32**, 1456-1465.
8. R. Dovesi, A. Erba, R. Orlando, C. M. Zicovich‐Wilson, B. Civalleri, L. Maschio, M. Rérat, S. Casassa, J. Baima and S. Salustro, *Wiley Interdisciplinary Reviews: Computational Molecular Science*, 2018, e1360.
9. C. F. Macrae, P. R. Edgington, P. McCabe, E. Pidcock, G. P. Shields, R. Taylor, M. Towler and J. v. d. J. J. o. A. C. Streek, 2006, **39**, 453-457.
10. V. G. Tsirelson, in *in The Quantum Theory of Atoms in Molecules: From Solid State to DNA and Drug Design*, eds. C. F. Matta and R. J. Boyd, Wiley-VCH Verlag GmbH & Co. KGaA, Weinheim, 2007, pp. 259-284.
11. A. V. Shishkina, V. V. Zhurov, A. I. Stash, M. V. Vener, A. A. Pinkerton and V. G. Tsirelson, *Crystal Growth Design*, 2013, **13**, 816-828.
12. B. Civalleri, K. Doll and C. M. Zicovich-Wilson, *The Journal of Physical Chemistry B*, 2007, **111**, 26-33.
13. A. M. Reilly and A. Tkatchenko, *The Journal of Physical Chemistry Letters*, 2013, **4**, 1028-1033.
14. G. J. Beran, *Chemical reviews*, 2016, **116**, 5567-5613.
15. S. F. Boys and F. Bernardi, *Molecular Physics*, 1970, **19**, 553-566.
16. B. Civalleri, C. M. Zicovich-Wilson, L. Valenzano and P. Ugliengo, *CrystEngComm*, 2008, **10**, 405-410.
17. I. Mata, I. Alkorta, E. Espinosa and E. Molins, *Chemical Physics Letters*, 2011, **507**, 185-189.
18. M. V. Vener, A. N. Egorova, A. V. Churakov and V. G. Tsirelson, *Journal of Computational Chemistry*, 2012, **33**, 2303-2309.
19. M. V. Vener, A. V. Shishkina, A. A. Rykounov and V. G. Tsirelson, *The Journal of Physical Chemistry A*, 2013, **117**, 8459-8467.
20. M. Rozenberg, A. Loewenschuss and Y. Marcus, *Physical Chemistry Chemical Physics*, 2000, **2**, 2699-2702.
21. A. N. Manin, A. P. Voronin, A. V. Shishkina, M. V. Vener, A. V. Churakov and G. L. Perlovich, *Journal of Physical Chemistry B*, 2015, **119**, 10466-10477.
22. A. O. Surov, A. V. Churakov and G. L. Perlovich, *Crystal Growth Design*, 2016, **16**, 6556-6567.
23. T. Gelbrich and M. B. Hursthouse, *CrystEngComm*, 2005, **7**, 324-336.
24. C. R. Groom, I. J. Bruno, M. P. Lightfoot and S. C. Ward, *Acta Crystallographica Section B*, 2016, **72**, 171-179.
25. A. Tilborg, G. Springuel, B. Norberg, J. Wouters and T. Leyssens, *CrystEngComm*, 2013, **15**, 3341-3350.
26. J. P. Merrick, D. Moran and L. Radom, *The Journal of Physical Chemistry A*, 2007, **111**, 11683-11700.
27. P. Ganguly and G. R. Desiraju, *CrystEngComm*, 2010, **12**, 817-833.
28. C. H. Görbitz, *Crystallography Reviews*, 2015, **21**, 160-212.
29. M. A. Spackman, P. Munshi and B. Dittrich, *ChemPhysChem*, 2007, **8**, 2051-2063.
30. E. V. Boldyreva, in *Models, mysteries and magic of molecules*, eds. J. C. A. Boeyens and J. F. Ogilvie, Springer, Dordrecht, 2008, pp. 167-192.
31. D. Braga, A. Angeloni, E. Tagliavini and F. Grepioni, *Journal of the Chemical Society, Dalton Transactions*, 1998, 1961-1968.
32. S. A. Katsyuba, M. V. Vener, E. E. Zvereva, Z. Fei, R. Scopelliti, J. G. Brandenburg, S. Siankevich and P. J. Dyson, *The Journal of Physical Chemistry Letters*, 2015, **6**, 4431-4436.

33. V. Bertolasi, P. Gilli, V. Ferretti and G. Gilli, *Journal of the American Chemical Society*, 1991, **113**, 4917-4925.
34. G. A. Jeffrey and W. Saenger, *Hydrogen bonding in biological structures*, Springer Science & Business Media, 2012.
35. C. Fonseca Guerra, F. M. Bickelhaupt, J. G. Snijders and E. J. Baerends, *Chemistry–A European Journal*, 1999, **5**, 3581-3594.
36. Y. Zhou, G. Deng, Y.-Z. Zheng, J. Xu, H. Ashraf and Z.-W. Yu, *J Scientific Reports*, 2016, **6**, 36932.
37. G. Gilli and P. Gilli, *Journal of Molecular Structure*, 2000, **552**, 1-15.